

InGaN/GaN QUANTUM ELECTROABSORPTION
MODULATORS WITH RECORD BREAKING
ELECTROABSORPTION IN BLUE

A THESIS

SUBMITTED TO THE DEPARTMENT OF ELECTRICAL AND

ELECTRONICS ENGINEERING

AND THE INSTITUTE OF ENGINEERING AND SCIENCES

OF BILKENT UNIVERSITY

IN PARTIAL FULFILLMENT OF THE REQUIREMENTS

FOR THE DEGREE OF

MASTER OF SCIENCE

By

Emre SARI

June 2007

I certify that I have read this thesis and that in my opinion it is fully adequate, in scope and in quality, as a thesis for the degree of Master of Science.

Assist. Prof. Dr. Hilmi Volkan Demir (Supervisor)

I certify that I have read this thesis and that in my opinion it is fully adequate, in scope and in quality, as a thesis for the degree of Master of Science.

Assist. Prof. Dr. Vakur Behçet Ertürk

I certify that I have read this thesis and that in my opinion it is fully adequate, in scope and in quality, as a thesis for the degree of Master of Science.

Assist. Prof. Dr. Fatih Ömer İlday

Approved for the Institute of Engineering and Sciences:

Prof. Dr. Mehmet Baray
Director of Institute of Engineering and Sciences

ABSTRACT

InGaN/GaN QUANTUM ELECTROABSORPTION MODULATORS WITH RECORD BREAKING ELECTROABSORPTION IN BLUE

Emre SARI

M.S. in Electrical and Electronics Engineering

Supervisor: Assist. Prof. Dr. Hilmi Volkan Demir

June 2007

Silicon based complementary metal-oxide-semiconductor (CMOS) technology has surely moved humankind forward in the information age. Over the years, Si CMOS has also evolved as the necessities of other technologies enabled by CMOS has expanded (for example, as the required speed of operation has increased). Consequently, CMOS microelectronics has been continuously replaced by their faster successors thus far. However, there is a physical limit to how fast conventional CMOS chips can run, constrained mainly due to the RC limitation of their electrical interconnects. This introduces a bottleneck in operating speed and even downscaling interconnects does not solve this problem. As a solution, optical clocking has been proposed and implemented commonly in the near infrared (NIR) where optoelectronic devices are readily available. But, silicon photodetectors fabricated in standard CMOS process unfavorably suffer from diffusion tail problem in NIR, which limits the operating speed, preventing direct high-speed clock injection into Si. To circumvent this problem, one approach is to utilize high-speed III-V photodetectors hybrid integrated on Si chips. This, however, introduces difficulties related to post-CMOS fabrication.

On the other hand, unlike in NIR, optical clock injection directly to Si is possible in the blue, where Si lacks the diffusion tail. However, there exists no chip-scale device particularly implemented to generate and inject optical clock signal blue to date. In this thesis, we propose blue InGaN/GaN based quantum electroabsorption modulators for a possible chip-scale solution to the modulation of blue clock signal. Here we present the device conception, design, growth, fabrication, experimental characterization, and theoretical analysis of these quantum electroabsorption modulators. Growing on polar *c*-plane of its wurtzite crystal, we obtain InGaN/GaN quantum structures with zig-zag potential profile due to alternating polarization-induced electrostatic fields and show that their absorption edge blue-shifts with applied electric field, unlike the red shift of conventional quantum confined Stark effect. In such InGaN/GaN quantum structures, we demonstrate the largest electroabsorption change of 6000 cm^{-1} (corresponding to 50 cm^{-1} absorption coefficient change for $1\text{ V}/\mu\text{m}$ field swing) around 424 nm ever reported for blue. This implies that the reversed quantum confined Stark effect in these InGaN/GaN quantum zigzag structures in the blue is comparable to the traditional quantum confined Stark effect in the InGaAsP/InP quantum well structures in NIR commercially used in communications. These proof-of-concept demonstrations show that blue InGaN/GaN quantum electroabsorption holds great promise for high-speed optical clock generation and injection directly into Si CMOS chips in the blue.

Keywords: electroabsorption, III-nitrides, modulator, wells, optical clocking.

ÖZET

MAVİ DALGABOYU ARALIĞINDA ELEKTROSOĞRULMA REKORU KIRAN InGaN/GaN KUVANTUM ELEKTROSOĞRULMA KİPLEYİCİLERİ

Emre SARI

Elektrik ve Elektronik Mühendisliği Bölümü Yüksek Lisans

Tez Yöneticisi: Yrd. Doç. Dr. Hilmi Volkan Demir

Haziran 2007

Hiç şüphesiz ki silisyum (Si) tabanlı tümleyici metal-oksit-yarıiletken (CMOS) teknolojisi yaşamakta olduğumuz iletişim çağında insanoğlunu ileriye taşıyan teknolojilerdendir. Yıllar geçtikçe Si CMOS da kullanıma açtığı teknolojilerin gereksinimlerinin (örneğin, gereken çalışma hızının) artmasıyla evrimleşti. Sonuç olarak CMOS mikroelektronik devreleri yerlerini daha hızlı varislerine bıraktı. Ancak, geleneksel CMOS yongalarının çalışma hızında temel bir fiziksel üst sınır vardır ve bu sınırın başlıca nedeni elektriksel arabağlantıların RC sınırlamasıdır. Bu çalışma hızında bir darboğaza yol açmakta olup arabağlantıların ölçekli küçültülmesiyle bile bu darboğaz aşılamamaktadır. Bir çözüm olarak, optik saatle denetim önerilmiş ve yaygın olarak optoelektronik aygıtların mevcut olduğu yakın kızılötesinde uygulanmıştır. Fakat silisyum tabanlı, örneğin standart CMOS teknolojisi ile üretilen, fotodetektörler yakın kızılötesinde istenmeyen bir şekilde difüzyon kuyruğu sorunu yaşamaktadır; bu da çalışma hızını düşürüp CMOS devrelere doğrudan optik saat denetimini engellemektedir. Bu sorunu

aşmak için önerilen çözümlerden biri, yüksek hızlı III-V fotodetektörleri silisyum yongalara melezleştirmektir. Ancak bu, CMOS-sonrası fabrikasyon gerektirmekte olup yonga üretimini zorlaştırmaktadır. Diğer yandan yakın kızılötesi yerine mavide optik saat denetim sinyalini üretmek ve silisyuma difüzyon problemi olmaksızın doğrudan sağlamak mümkündür. Ancak şu ana kadar mavi dalgaboyu aralığında optik saat denetim sinyalinin üretilmesi ve silisyuma doğrudan sağlanması için yonga ölçekli bir aygıt yapılmamıştır. Bu tezde mavi saat denetim sinyalinin üretimi için olası bir yonga ölçekli aygıt çözümü olarak InGaN/GaN tabanlı kuvantum elektrosöğrulme kipleycilerini sunuyoruz. Burada aygıtlarımızın tasarımı, büyütülmesi, fabrikasyonu, deneysel karakterizasyonu ve kuramsal analizi sunuluyor. Sahip olduğu wurtzite kristal yapısının kutuplu c-düzlemine büyüttüğümüz InGaN/GaN kuvantum yapılarında kutuplama-sebepli zıt yönlü elektrostatik alanlarından dolayı zig-zag potansiyel profili gözlemliyoruz ve söğrulme bant kenarının uygulanan elektrik alanla maviye kaymaya ugradığını deneysel ve teorik olarak gösteriyoruz. InGaN/GaN kuvantum yapılarında en yüksek 6000 cm^{-1} lik bir söğrulme katsayısı değişimi ($1 \text{ V}/\mu\text{m}$ elektrik alan değişimine karşılık 50 cm^{-1} söğrulme sabiti değişimi) elde etmekteyiz. Bu, gözlemlediğimiz tersine kuvantum sınırlamalı Stark etkisinin iletişim sektöründe ticari olarak kullanılan ve yakın kızılötesinde çalışan InGaAsP/InP tabanlı kuvantum kuyu yapılarındaki geleneksel kuvantum sınırlamalı Stark etkisi kadar güçlü olduğunu göstermektedir. Yapılabilirliğini gösterdiğimiz mavi InGaN/GaN kuvantum elektrosöğrulme kipleycileri mavi dalgaboyu aralığında yüksek hızlı saat denetim sinyalini üretimi ve silisyum tabanlı CMOS yongalara doğrudan sağlanması için ümit vadetmektedir.

Anahtar Kelimeler: elektrosöğrulme, III-nitrürler, kipleyci, kuyular, optik saat denetimi

ACKNOWLEDGMENTS

First, I would like to express my gratitude to my supervisor Prof. Hilmi Volkan Demir for his endless support (in all aspects), guidance and motivation. It is an honor and a great experience to be working with him. Also thanks to all other Demir group members.

I would also like to thank Prof. Ekmel Ozbay for initiating Nanotam, a center of excellence and his former and present group members for their help during my growth, fabrication and characterization training.

Thanks to Prof. In-Hwan Lee for his interest to our work. I think we will do a lot more in this collaboration.

I would like to thank Profs. Vakur B. Erturk and F. Omer Ilday for their helpful comments to this thesis.

I'd like to acknowledge TUBITAK for support during my M.S. studies.

Finally I would like to express my love to my family for always being there for me.

Contents

1	INTRODUCTION	1
1.1	Problem Statement	1
1.2	Motivation	2
1.2.1	Device Perspective	2
1.2.2	Materials Perspective	3
1.3	Objective	4
1.4	Summary	4
2	III-NITRIDE SEMICONDUCTOR MATERIAL	6
2.1	Crystal Structure of III-Nitrides	6
2.2	Quantum Heterostructures of III-Nitrides	7
2.3	Growth of III-Nitrides	11
2.3.1	Metal Organic Chemical Vapor Deposition of III-Nitrides	12
3	PHYSICS of OPTICAL ELECTROABSORPTION	13

3.1	Optical Absorption in Semiconductors	13
3.2	Electroabsorption Mechanisms	16
3.2.1	Franz-Keldysh Effect	16
3.2.2	Quantum Confined Stark Effect	18
3.3	Quantum Electroabsorption Modeling	20
3.3.1	Transfer Matrix Method and Its Implementation	22
3.3.2	Theoretical Demonstration of Quantum Confined Stark Ef- fect Using Transfer Matrix Method	26
4	DEVICE IMPLEMENTATION	28
4.1	Design Work	28
4.1.1	Quantum Design	28
4.1.2	Epitaxial Design	31
4.1.3	Device Design	32
4.2	Experimental Work	33
4.2.1	Growth	33
4.2.2	Material Characterization	34
4.2.3	Fabrication	38
4.2.4	Device Characterization	39
5	CONCLUSIONS AND FUTURE DIRECTIONS	49

<i>CONTENTS</i>	viii
5.1 Conclusions	49
5.2 Future Directions	50
APPENDIX	52
A TRANSFER MATRIX METHOD	52

List of Figures

1.1	Absorption spectra and penetration depth of various semiconductors (After Ref. [5]).	2
1.2	Electroabsorption modulator device concept (After Ref. [7]).	3
1.3	Absorption band edges of III-nitrides in the optical spectrum [9].	4
2.1	Wurtzite crystal of GaN. White atoms can either be Ga or N, depending on the polarity (After Ref. [9]).	7
2.2	Electric field intensity (in MV/cm), in an $In_xAl_yGa_{1-x-y}N/GaN$ quantum structures same thickness in well and barrier: (a) our results (black line indicates zero field cases) and (b) After Ref. [11]	10
2.3	A representative band diagram of $In_{0.1}Ga_{0.9}N/GaN$ quantum zigzag structure we obtained by combining the available material parameters and electric field calculations.	11
3.1	Band-to-band absorption in semiconductors (After Ref. [15]).	14
3.2	A p-i-n photodiode under reverse bias and illumination (After Ref. [16]).	14
3.3	Basic concept of Franz-Keldysh effect (After Ref. [14])	17

3.4	Basic concept of quantum confined Stark effect. (After Ref. [14])	19
3.5	Optical absorption spectra for $AlGaAs/GaAs$ quantum well structure for various electric fields applied perpendicular to quantum well layers measured at room temperature. The spectra are shifted vertically to dashed levels for clarity. (After Ref. [14])	20
3.6	Implementation of the tunneling resonance method using bisection method (After Ref. [14]).	23
3.7	Associated energy eigenstates for Quantum Structure 1, obtained by our TMM-based simulation tool.	24
3.8	Associated energy eigenstates for quantum structure 2, obtained by our TMM based simulation tool.	25
3.9	Associated electron eigenstates and energy eigenvalues for $Al_{0.3}Ga_{0.7}As/GaAs$ quantum structure obtained by our TMM based simulation tool (wavefunctions are normalized to different values for visualization purposes).	26
3.10	Absorption spectra for $Al_{0.3}Ga_{0.7}As/GaAs$ quantum structure for different external electric field intensities obtained by our TMM based simulation tool.	27
4.1	Wavefunctions of $In_{0.1}Ga_{0.9}N/GaN$ quantum structures that we calculate using TMM for zero and non-zero external electric field cases.	29
4.2	Absorption spectra for $In_{0.1}Ga_{0.1}N/GaN$ quantum structures that we calculate using TMM.	30
4.3	Layout program view of a modulator in our photomask design. . .	32

4.4	Layout program view of TLM grids in our photomask design. . . .	32
4.5	In-situ reflectivity measurement results for <i>InGaN/GaN</i> quantum electroabsorption modulator wafer at $\lambda=541.4$ nm where the wafer is transparent.	34
4.6	$0.5 \mu\text{m} \times 0.5 \mu\text{m}$ atomic force microscope image taken from one of our wafers.	35
4.7	Photoluminescence spectrum of one of our epi-wafers	36
4.8	A typical wafer transmission spectrum for our <i>InGaN/GaN</i> quantum electroabsorption modulators.	36
4.9	SIMS analysis results of one of our wafers with 15 <i>InGaN/GaN</i> quantum well/barrier structures.	37
4.10	Device after cleaning.	38
4.11	Device after mesa etching.	38
4.12	Device after p-contact formation.	39
4.13	Device after n-contact formation and annealing.	39
4.14	Micrograph of a fabricated device.	40
4.15	IV curve of one of our modulators, inset shows the semilog scale IV characteristics.	40
4.16	Electroluminescence spectrum of one of our modulators.	41
4.17	Electroabsorption test setup.	42
4.18	Electroabsorption spectra of 4 nm/4 nm <i>InGaN/GaN</i> quantum modulators. Inset shows the 0 V absorption curve separately. . . .	42

4.19	Absorption coefficient change with respect to 0 V absorption. Inset shows the transmission spectrum for 0 and 5 V reverse bias.	44
4.20	Field direction dependent demonstration of reversed and traditional quantum confined Stark effect. E denotes the external electric field and P denotes the polarization-induced electrostatic field inside the quantum well.	45
4.21	Electroabsorption spectra of 2.5 nm/7.5 nm <i>InGaN/GaN</i> field direction dependent experimental demonstration of reversed and traditional quantum confined Stark effect.	46
4.22	Absorption coefficient change with respect to 0 V absorption for the device of 2.5 nm/ 7.5 nm quantum structure. Inset shows the 0 V and 10 V absorption curves separately.	46
4.23	Electroabsorption spectra of the device that operates 485 nm for various reverse bias voltage levels. Inset shows the same of 1 V and 5 V bias in a wider spectrum showing a low level of excitonic effects.	47
4.24	Absorption coefficient change with respect to 2 V absorption for the device optimized for 485 nm wavelength of operation.	48
5.1	Dominant mode E-field profile for one of our rib waveguide designs (in collaboration with M. Yorulmaz of our group).	50
5.2	Scanning electron micrograph obliquely taken from one of our devices (etched in RIE).	51
A.1	Discretization of potential profiles in TMM.	52
A.2	Transfer matrix method nomenclature (After Ref. [14]).	53

A.3 Definition of waves for an arbitrary layer in TMM (After Ref. [14]) 53

List of Tables

2.1	Calculated built-in electrostatic fields for some III-nitride quantum structures	9
3.1	Energy eigenvalue results obtained by different methods for Quantum Structure 1.	24
3.2	Energy eigenvalue results obtained by different methods for quantum structure 2	25
4.1	A representative epitaxial design.	31

Şımarıklıklarına inatla sabır ve sevgi gösteren aileme...

Chapter 1

INTRODUCTION

1.1 Problem Statement

Today silicon microelectronics is limited in operating speed. The electrical interconnects suffer from the RC limitation¹ and scaling does not mitigate this problem [1]. High speed electrical signals (e.g., data or clock) are subject to delays of significant fractions of one clock period and this causes severely limiting electrical effects such as jitter and skew. This leads to a bottleneck in electrical clocking and interconnection. Using optical pulses for these purposes is proposed as a remedy [2].

Thus far, optical clock distribution has been commonly implemented in the near infrared (NIR) spectral region where high performance optoelectronic devices (e.g., in III-arsenide and III-phosphite) are readily available [3]. However, silicon photodetectors, for example, those fabricated in standard complementary metal-oxide-semiconductor (CMOS) process, unfavorably exhibit very low optical absorption (and very long penetration depth), as shown in Fig. 1.1 and thus suffer a diffusion tail, with long response time, in this spectral region [4]. This limits the operating speed of Si CMOS photodetectors to ~ 1 Gbits/s. To circumvent this problem, one approach is to utilize

¹e.g., resistance per unit length (for metal lines that carry data and clock signals) increases with frequency by skin effect.

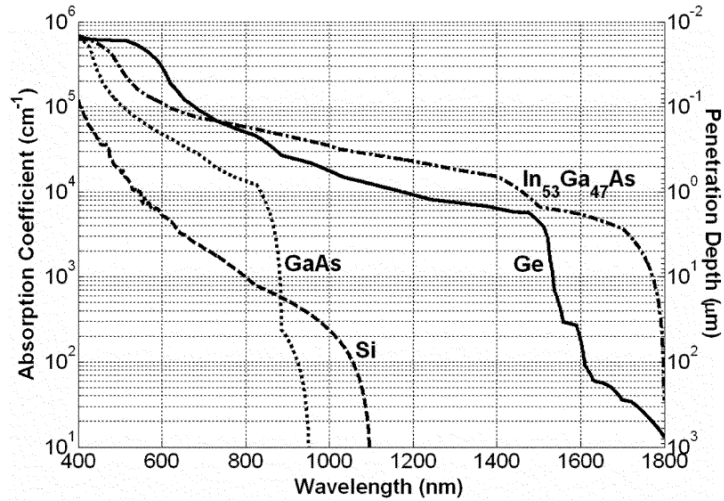


Figure 1.1: Absorption spectra and penetration depth of various semiconductors (After Ref. [5]).

high-speed NIR (e.g., $In_{0.53}Ga_{0.47}As$) photodetectors hybrid integrated on Si chips. This, however, introduces difficulties related to post-CMOS fabrication.

1.2 Motivation

Unlike in the NIR, optical clock injection directly into Si-based microelectronic circuits via Si-based photodetectors is possible (without violating the CMOS process) by generating optical clock signals in the blue, where Si features a short penetration depth (100 nm at ~ 400 nm) as given in Fig. 1.1. Si, in this spectral region, lacks diffusion tail and thus beats the responsivity-speed tradeoff [4]. To date, no *chip-scale* device implemented to create blue clock signals at high speeds has been reported. Such a device would help to fill the gap between optics and Si-based CMOS electronics and be a feasible solution for CMOS clocking problem.

1.2.1 Device Perspective

For applications that require compactness and high repetition rates (e.g., ~ 10 GHz) in optical signal generation, it is customary to use electroabsorption modulators (EAM)

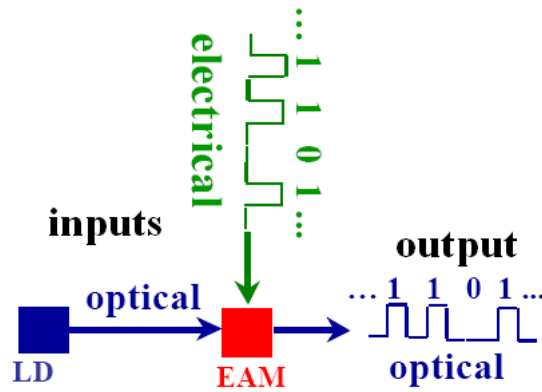


Figure 1.2: Electroabsorption modulator device concept (After Ref. [7]).

along with continuous wave (cw) laser diodes. Electroabsorption modulators are devices that mix an electrical signal with an optical carrier, the carrier frequency being the optical frequency [6]. A schematic that illustrates the device concept of electroabsorption modulators is given in Fig. 1.2.

An important figure of merit for EAMs is the *contrast ratio* (CR), the ratio of optical power level of the binary bit “1” to that of the bit “0”. This figure of merit affects the receiver’s ability to distinguish each bit and thus the bit error rate (BER). Contrast ratio is usually expressed in dB as given in Eq. (1.1). Although a contrast ratio of 3 dB is demonstrated to be sufficient for applications with short distance optical pulse propagation [8], such as in optical clocking and interconnection, , a CR of >10 dB is desirable for system applications.

$$CR = 10 \left| \log_{10} \left(\frac{P_1}{P_0} \right) \right| \quad (1.1)$$

1.2.2 Materials Perspective

Since the demonstration of the first *InGaN/GaN*-based blue light emitting diode (LED) in 1993, there has been an enormous technical interest in III-nitride material system. This interest has increased as green to near-ultraviolet LEDs were commercialized and the first blue laser diode was demonstrated. Since then, many electronic²

²e.g., High power high electron mobility transistors (HEMTs)

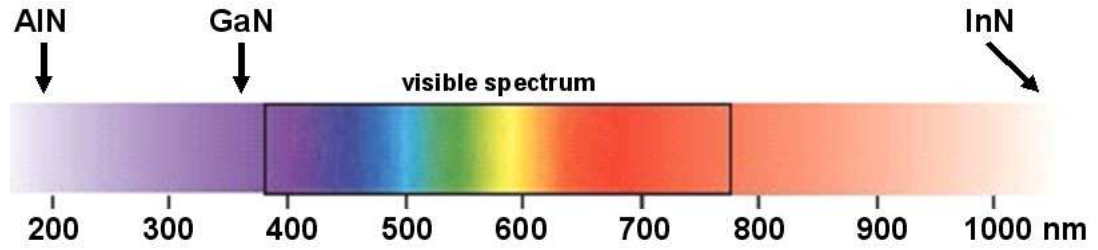


Figure 1.3: Absorption band edges of III-nitrides in the optical spectrum [9].

and optoelectronic³ devices and systems⁴ have been rapidly-successfully demonstrated and many of them were commercialized.

This rapid improvement and interest stem from the unique properties that this material system offers. Since III-nitrides are direct bandgap materials, they are very useful for optoelectronic devices. Also, using their alloys, a very large wavelength region (from ~ 200 nm for *AlN* to longer than 1200 nm for *InN*) that includes the whole visible spectrum can be spanned.

1.3 Objective

Our main objective in this thesis is to investigate III-nitride based quantum electroabsorption modulators as a new chip-scale optoelectronic device for optical clock generation and understand the underlying physics behind them. We also aim at studying the device properties through engineering quantum structures for a stronger electroabsorption effect. We further target at developing a strong know-how in III-nitride device design and implementation.

1.4 Summary

This thesis is organized as follows. In Chapter 2, we review basic material properties of III-nitrides and present a brief overview of their quantum heterostructures and growth.

³e.g., blue laser diodes, white, blue and green LEDs, solar-blind photodetectors

⁴e.g., BluRay DVD drives, *AlGaIn/GaN* HEMT power amplifiers

In Chapter 3, we provide a background on optical electroabsorption by explaining basic electroabsorption mechanisms. In this chapter we also introduce transfer matrix method, a powerful technique that was used in our analysis of quantum heterostructures. In Chapter 4, we present our theoretical and experimental work on the design and implementation of our InGaN/GaN based blue quantum electroabsorption modulators. In the last chapter we conclude by summarizing our accomplishments and give an outlook about our future directions.

Chapter 2

III-NITRIDE SEMICONDUCTOR MATERIAL

As mentioned in the first chapter, III-nitrides are direct bandgap semiconductors with alloys ($In_xAl_yGa_{1-x-y}N$, $0 \leq x, y, x + y \leq 1$) of bandgap energies spanning a very wide range of optical spectrum. As a result, not only III-nitride platform serves today's high-tech industry by its optoelectronic devices demonstrated so far, but it also holds a great promise for new ones. To design and demonstrate new III-nitride devices for their respective applications, it is essential to understand their material properties. This chapter deals primarily with these properties and explains how to engineer them using quantum heterostructures, along with their growth using metal organic chemical vapor deposition technique.

2.1 Crystal Structure of III-Nitrides

Group III-nitrides are found in three different crystal structures being zincblende, rocksalt and wurtzite. Among these, primarily because of the obtained high crystal

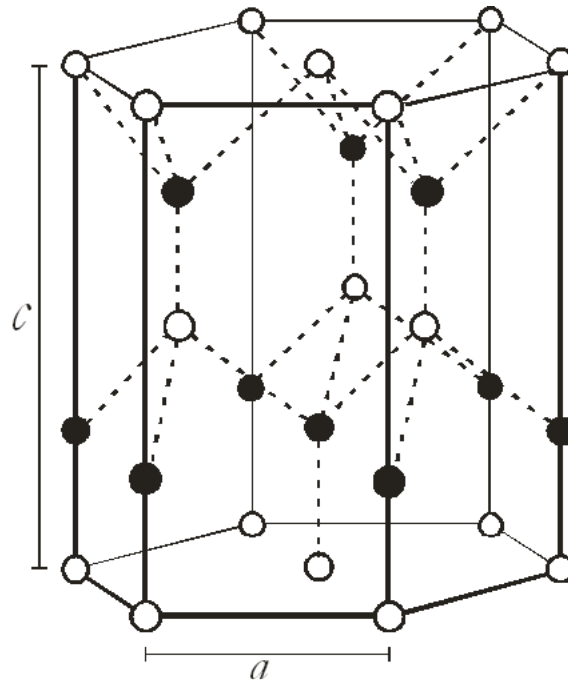


Figure 2.1: Wurtzite crystal of GaN. White atoms can either be Ga or N, depending on the polarity (After Ref. [9]).

quality and the relative ease of growth, wurtzite is the dominant one. Wurtzite crystal structure is characterized by the lattice parameters a and c . This configuration, e.g., for GaN consists of alternating biatomic closed-packed (0001) planes of Ga and N pairs stacked in an alternating sequence [9] as shown in Fig. 2.1. Atoms in the first and third layer are symmetrically aligned with each other. As seen in Fig. 2.1, wurtzite structure does not have an inversion plane perpendicular to the c -axis. Thus the surfaces of the crystals grown on c -plane have either a Group III element (Al, Ga or In) polarity or an N polarity. The influence of this polarization will be discussed later in this chapter.

2.2 Quantum Heterostructures of III-Nitrides

Semiconductor heterostructure is formed by two types of interfacing semiconductors (i.e., in heterojunctions) to achieve characteristics that are not feasible in either type of the materials separately. By simply cascading (at least two of) such structures

very close to each other (about a few nanometers), it is possible to form quantum heterostructures (wells and barriers), which render very interesting quantum effects from a device point of view.

As mentioned earlier, wurtzite III-nitrides have a polarity along their c-axis (i.e., [0001]) and this is the conventional growth axis. Due to low crystal symmetry and deviation of lattice parameters, intrinsic (spontaneous) polarization is observed even in their bulk form. The direction of this polarization field always points from metal atom to N atom [9]. Because of the discontinuity of total polarization, sum of spontaneous polarization (\mathbf{P}_{sp}), and relatively strong strain-induced piezoelectric polarization (\mathbf{P}_{pz}) fields, built-in sheet charges of very large density are induced in their heterojunctions¹. The density of these sheet charges (σ) can exceed $\pm 10^{13} \text{cm}^{-2}$ [10]. In quantum heterostructures, the same effect is observed as built-in electric fields of huge intensity. Since this is an intrinsic effect, it must cause no potential built up over the whole well-barrier structure and this can be used as a boundary condition in their analysis [11].

From a circuit theory point of view, they form a structure very similar to a series of parallel plate capacitors. Charges on each capacitor plate and the voltage drop on each capacitor alternates in sign and they are equal in absolute value, due to charge neutrality and zero voltage build-up conditions imposed by the circuit.

Spontaneous polarization field, \mathbf{P}_{sp} , is known for bulk *GaN*, *AlN* and *InN*. For their alloys, this is estimated by a Vegard-like rule (i.e., linear interpolation) [11]. Strain-induced piezoelectric polarization, \mathbf{P}_{pz} , expression is given as follows [12]:

$$\mathbf{P}_{pz} = \overleftarrow{e} \cdot \overrightarrow{\epsilon} \quad (2.1)$$

where \overleftarrow{e} is the piezoelectric constants tensor and $\overrightarrow{\epsilon}$ is the strain field of the material, which can both be estimated by the linear interpolation.

¹In the literature, this is referred to as two-dimensional electron/hole gas (2DEG, 2DHG).

Under the mentioned boundary condition, we obtain the built-in electrostatic field intensities for multiple quantum well structures as follows:

$$\mathbf{E}_{tot}^{well} = \mathbf{E}_{sp}^{well} + \mathbf{E}_{pz}^{well} = \frac{(\mathbf{P}_{sp}^{barrier} + \mathbf{P}_{pz}^{barrier}) - (\mathbf{P}_{sp}^{well} + \mathbf{P}_{pz}^{well})}{\epsilon_{well} + \frac{d_{well}}{d_{barrier}} \epsilon_{barrier}} \quad (2.2)$$

and

$$\mathbf{E}_{tot}^{barrier} = \mathbf{E}_{sp}^{barrier} + \mathbf{E}_{pz}^{barrier} = \frac{(\mathbf{P}_{sp}^{well} + \mathbf{P}_{pz}^{well}) - (\mathbf{P}_{sp}^{barrier} + \mathbf{P}_{pz}^{barrier})}{\epsilon_{barrier} + \frac{d_{barrier}}{d_{well}} \epsilon_{well}} \quad (2.3)$$

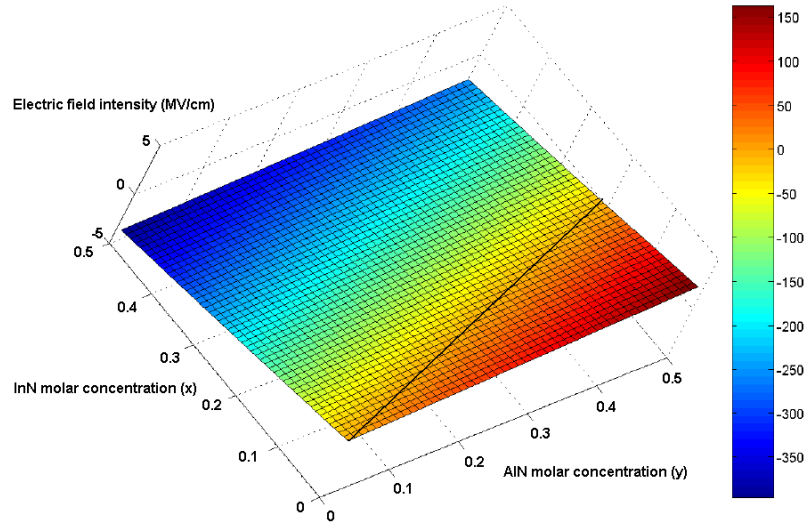
Using these expressions and relevant material parameters available in the literature, we calculate the built-in electrostatic fields in some of polar III-nitride quantum multiple well structures as listed in Table (2.1).

Table 2.1: Calculated built-in electrostatic fields for some III-nitride quantum structures

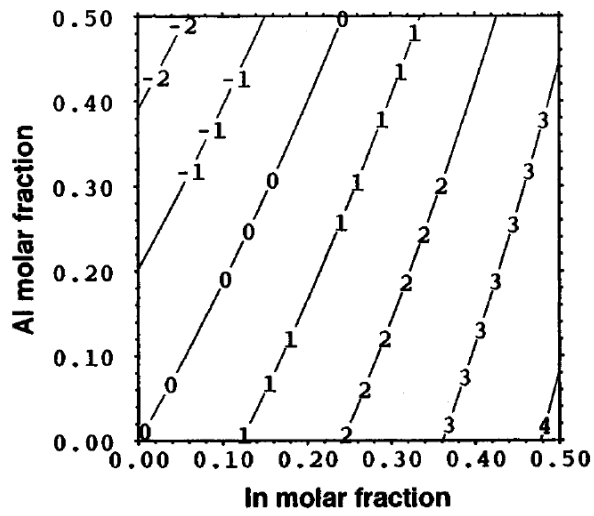
Well	Barrier	d_{well}	d_{bar}	E_{well}	E_{bar}
$In_{0.05}Ga_{0.95}N$	GaN	4 nm	4 nm	-88.1 V/ μm	88.1 V/ μm
$In_{0.1}Ga_{0.9}N$	GaN	4 nm	4 nm	-175.4 V/ μm	175.4 V/ μm
$In_{0.1}Ga_{0.9}N$	GaN	4 nm	6 nm	-209 V/ μm	139 V/ μm
$In_{0.1}Ga_{0.9}N$	GaN	4 nm	∞	-340 V/ μm	0 ⁺ V/ μm
GaN	$Al_{0.1}Ga_{0.9}N$	4 nm	6 nm	-87.2 V/ μm	58 V/ μm
GaN	$In_{0.1}Al_{0.9}N$	4 nm	6 nm	-610.4 V/ μm	406.9 V/ μm
GaN	$In_{0.11}Al_{0.287}Ga_{0.603}N$	4 nm	4 nm	0 V/ μm	0 V/ μm

As seen in Table (2.1), and intuitively from Eq.s (2.2) and (2.3), the electrostatic field inside the quantum well decreases with the well-to-barrier width ratio (d_{well}/d_{bar}) and with the mismatch between well and barrier layers. We have polarization-induced electrostatic fields with lower intensities for $AlGaN/GaN$ quantum structures compared to $InGaN/GaN$ quantum structures. Also, in principle, with the appropriate InN and AlN molar concentrations, it is possible to achieve zero built-in electrostatic fields inside both wells and barriers². When we compare our calculation results of these built-in electrostatic fields, we observe that they perfectly match with the other theoretical results in the literature as depicted in Fig. 2.2. To produce new devices with quantum structures in III-nitride platform, one has to carefully consider these fields in his design.

²However, the growth of such quaternary alloys is very difficult.



(a)



(b)

Figure 2.2: Electric field intensity (in MV/cm), in an $In_xAl_yGa_{1-x-y}N/GaN$ quantum structures same thickness in well and barrier: (a) our results (black line indicates zero field cases) and (b) After Ref. [11]

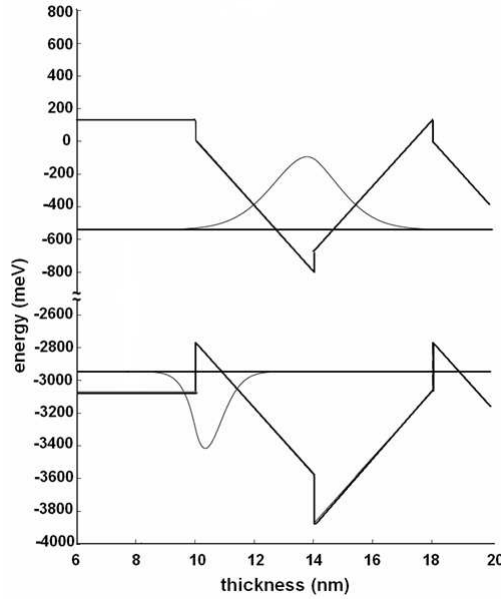


Figure 2.3: A representative band diagram of $In_{0.1}Ga_{0.9}N/GaN$ quantum zig-zag structure we obtained by combining the available material parameters and electric field calculations.

Additionally, using bandgap energy values of InN , GaN , and AlN , and conduction and valence band offsets for their heterostructures, we obtain the band diagram of any c-plane (polar) III-nitride quantum structure, one of which is depicted in Fig. 2.3 for $In_{0.1}Ga_{0.9}N/GaN$ quantum structure as an example.

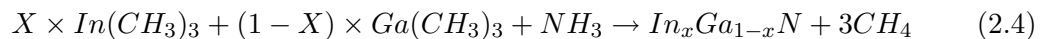
2.3 Growth of III-Nitrides

There are several different techniques for the growth of III-Nitrides. Metal organic chemical vapor deposition (MOCVD), molecular beam epitaxy (MBE) and hydride vapor phase epitaxy (HVPE) are the most popular ones amongst all. As a common property of these methods, it is much more convenient and easier to grow c-plane Ga-face GaN . However, and unfortunately, there has been no feasible technique for the synthesis of a native substrate for this material's growth, at least until now. So, heteroepitaxy is a must for the growth of these materials [9].

Due to their low lattice mismatch and/or thermal expansion coefficient mismatch to GaN , the most commonly used substrates are sapphire (Al_2O_3), silicon (Si), and silicon carbide (SiC) [9]. By growing a thick GaN layer on these substrates in appropriate conditions, one can get a crystalline GaN , with a reasonably high quality. For all of our devices, we use MOCVD technique and grow the epitaxial structures on the c-plane sapphire and obtain Group III-face crystals.

2.3.1 Metal Organic Chemical Vapor Deposition of III-Nitrides

MOCVD is the most popular technique of producing GaN based high power light emitting diodes (LEDs) that have been commercially available for about 13 years [13]. The technique is based on the deposition of atoms that are set free by chemical reactions that occur at high temperatures ranging from $500^\circ C$ (for InN) to $1200^\circ C$ (for AlN). These reactions take place between metal organic vapors (group-III material sources) and hydrides (the nitrogen sources). These substances are called precursors. The precursors commonly used in MOCVD growth of $In_xAl_yGa_{1-x-y}N$ semiconductors are three-methyl gallium (TMGa or $Ga(CH_3)_3$), three-ethyl gallium (TEGa or $Ga(C_2H_5)_3$), three-methyl aluminum (TMAI or $Al(CH_3)_3$), three-methyl indium (TMIn or $In(CH_3)_3$) and ammonia (NH_3). For the n- and p-doped growth of III-nitrides, silane (SiH_4) and bis-cyclopentadienylmagnesium ($CpMg_2$) are used, respectively. A representative chemical reaction between the precursors is given in (2.4):



By intentionally slowing down this reaction and reducing the MOCVD growth rate (to ~ 1 nm/minute), one can achieve high-quality GaN-based quantum structures in a controlled manner.

Chapter 3

PHYSICS of OPTICAL ELECTROABSORPTION

This chapter deals primarily with the physics of optical absorption and electroabsorption in semiconductors. It also introduces two main electroabsorption mechanisms (Franz-Keldysh and quantum confined Stark effects) and a quantum mechanical method to analyze the quantum electroabsorption.

3.1 Optical Absorption in Semiconductors

In semiconductors, optical absorption is generally referred to as the generation of a photocarrier (electron-hole) pair as response to an incident photon. For the case of most semiconductor structures and photon energies, this carrier generation usually occurs between the conduction band and the valence band as depicted in Fig. 3.1. The likelihood of this event is proportional to the probability of finding an electron in the conduction band and a hole in the valence band in the same vicinity [14].

For indirect bandgap semiconductors, this process must usually be assisted by phonon emission to conserve momentum during this process, whereas for direct

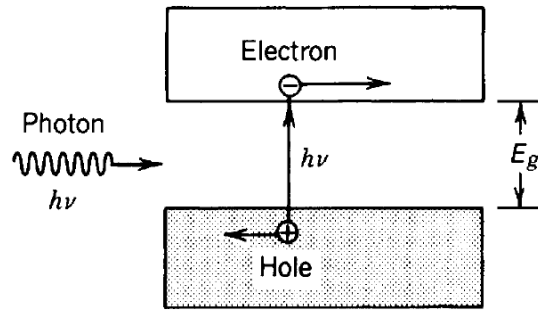


Figure 3.1: Band-to-band absorption in semiconductors (After Ref. [15]).

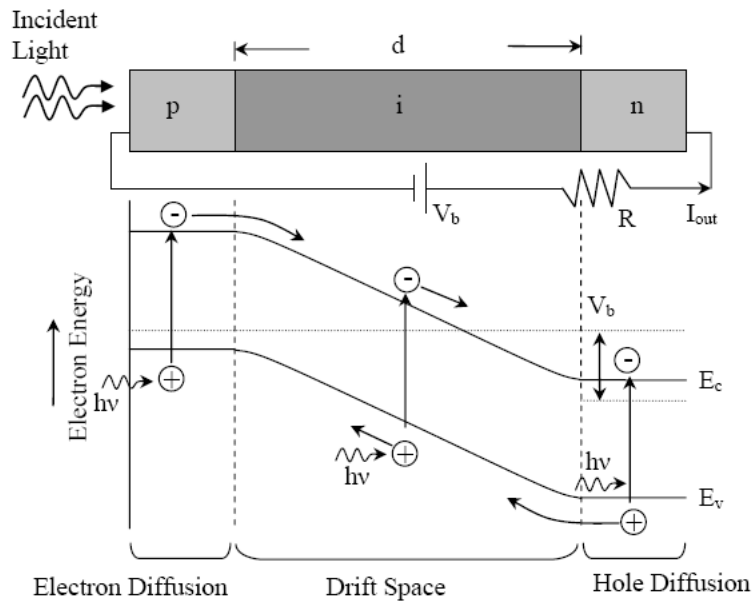


Figure 3.2: A p-i-n photodiode under reverse bias and illumination (After Ref. [16]).

bandgap semiconductors phonons are not involved in the optical transition. Photodiodes (e.g., photodetectors and electroabsorption modulators) are usually operated at reverse bias voltages. Generated photocarrier pairs are collected through the drift process and they contribute to reverse bias current as illustrated in Fig. 3.2.

There are a number of definitions that help us examine the properties and performance of such devices in this context. The first definition is the quantum efficiency, η , which is the probability that a single photon, incident on the device, generates an electron-hole pair that contributes to the photodiode current (i.e., photocurrent). In a statistical point of view, η is the ratio of the flux of generated electron-hole pairs

that contribute to the photocurrent (Φ_e) to the flux of photons incident on the device (Φ_p) [15]. The generic expression of quantum efficiency is given as:

$$\frac{\Phi_e}{\Phi_p} \triangleq \eta = (1 - R)\zeta(1 - e^{-\alpha d}) \quad (3.1)$$

The first factor, $(1-R)$, in the right hand side of this expression represents the ratio of photons that make it into the device (i.e., transmission coefficient), in other words the ones that survive through Fresnel reflection, R . The second factor, ζ , represents the ratio of electron-hole pairs that successfully contribute to photocurrent. And the third factor represents the fraction of photon flux absorbed in the active (absorbing) region of the device, coming from the model that formally explains this process as an exponential attenuation with the defined absorption constant, α [15].

Another definition for such devices is the responsivity \mathfrak{R} , which is the ratio of photocurrent, i_p , to the incident optical power, P_o . By using the expressions of optical power and photocurrent relating to photon and electron flux, respectively, we arrive at the following expression for \mathfrak{R} that relates to η :

$$\mathfrak{R} = \frac{i_p}{P_o} = \frac{\eta e}{h\nu} = \eta \frac{\lambda}{1.24} \quad (3.2)$$

where λ is the wavelength given in μm and \mathfrak{R} is given in A/W.

By combining Eq.s (3.1) and (3.2) and assuming a constant Fresnel reflection coefficient, R , and a constant ζ over a spectrum, we arrive at the following compact formula that spectrally relates i_p and P_o to α for a certain structure having an active layer thickness of d :

$$\alpha = -\frac{1}{d} \ln \left(1 - \frac{i_p}{P_o \lambda} \frac{1.24}{\zeta(1 - R)} \right) \quad (3.3)$$

As mentioned earlier, these definitions are very helpful for examining the device performance and for understanding the physics of such devices, especially electroabsorption modulators.

3.2 Electroabsorption Mechanisms

Electroabsorption is the phenomenon where absorption characteristics of a material changes in response to an externally applied electric field, \mathbf{E} . This phenomenon is usually utilized by a few mechanisms in semiconductors. These mechanisms are interesting and important for practical purposes because they enable optoelectronic modulators, which are the key elements in optical communications.

Electroabsorption mechanisms merely require an electric field to be applied across a semiconductor and this is usually achieved within a reverse biased diode structure. Their operating speed is generally limited by RC time constants of themselves (due to parasitic resistance and device capacitance) since neither population inversion nor carrier injection is required for these effects to take place. So the speed issues are not affected by the time constants associated with carrier population changes and hence it is possible to utilize them for high speed operation by good device engineering.

3.2.1 Franz-Keldysh Effect

As the first of such mechanisms, we start investigating Franz-Keldysh effect (FKE). The Franz-Keldysh effect is observed in bulk semiconductors where conduction and valence bands can be viewed as to be tilted when an external electric field is applied. By the application of the electric field, electrons and holes can tunnel into conduction and valence bands, respectively [14]. Photons having slightly less energy than the bandgap energy, E_g , of the semiconductor can be absorbed by this tunneling - whereas this cannot be the case when no electric field is applied and excitonic effects (i.e., Coulomb interaction between electron and holes) are neglected. The basic mechanism of FKE is depicted in Fig. 3.3.

It is possible to notice from the visual description of FKE that the probability of finding an excess electron and hole in the same vicinity (quantitatively, absolute

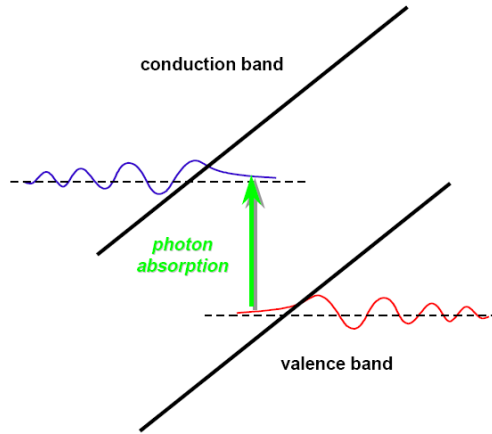


Figure 3.3: Basic concept of Franz-Keldysh effect (After Ref. [14])

squared-overlap integral of normalized electron and hole wavefunctions), which is proportional to the absorption level, is much less than 1 for any case. Hence, the dependence of absorption coefficient on the \mathbf{E} -field intensity is very low. It is also apparent that absorption edge, the longest wavelength at which absorption occurs, shifts to longer wavelengths (i.e., redshifts) when electric field is applied regardless of the direction of the \mathbf{E} -field.

As mentioned earlier, when light propagates through the semiconductor its intensity decays exponentially with a “length constant” of $1/\alpha$. α is the absorption constant and is a function of photon energy (i.e., wavelength), and now \mathbf{E} field. However, as qualitatively explained, it is not a strong function of electric field for bulk semiconductors. As a typical value, $\sim 2 \text{ cm}^{-1}$ of absorption coefficient change is achievable by an electric field change of $1 \text{ V}/\mu\text{m}$ in the transparent region of GaN [17].

From a device point of view, for a good electroabsorption modulator operation, it is essential to have a large absorption coefficient change with a moderate level of voltage swing across the device. The FKE can give considerably good device operation in terms of contrast ratio when waveguide architecture is utilized, where optical interaction with the active medium is increased. But in lumped RC operation, these devices are usually beaten by speed issues due to requirements of high voltage change and long waveguides, latter being related to parasitic device capacitance, (unless used in distributed RC operation [e.g., traveling wave modulators]).

As a confirmation of this conclusion, experimental studies and theoretical analysis available in the literature (even the ones that take excitonic effects into account) show that it is not easy to have a large contrast ratio for very high speeds using a bulk electroabsorption modulator utilizing FKE. There has been a moderate number of modulators reported utilizing FKE that operate in near infrared [18] and near UV range [19].

3.2.2 Quantum Confined Stark Effect

Another and much stronger electroabsorption mechanism in semiconductors is the quantum-confined Stark effect (QCSE), which is the quantized version of FKE.

Quantum heterostructures (wells, wires and dots), having confined dimension(s) of the order of one Bohr exciton radius (a few nanometers), exhibit very strong excitonic properties such as strong photoluminescence (PL) peaks at room temperature, and sharp absorption edges [14]. Theoretical and experimental studies have shown that these structures possess strong electroabsorption properties when electric field is applied perpendicular to the confined dimension(s). Similar to FKE, absorption edge shifts to longer wavelengths (i.e., redshifts) as the applied \mathbf{E} field is increased [14]. This mechanism is depicted for a GaAs-like (in terms of electron and hole effective masses) infinite quantum well in Fig. 3.4.

There are a couple of remarks to note in the visual description of QCSE. First, electron and hole are pulled in opposite directions by the \mathbf{E} field and electron and hole wavefunctions at first energy states overlap relatively less for $\mathbf{E} \neq \mathbf{0}$ case. Second, previously forbidden-like transitions are allowed with the application of \mathbf{E} field, in other words electron and hole wavefunctions at other energy states are not orthogonal anymore. Also, absolute-squared overlap integral of normalized non-orthogonal electron and hole wavefunctions for $\mathbf{E} \neq \mathbf{0}$ case is close to 1, but not as large as $\mathbf{E} = \mathbf{0}$ case - in agreement with the sum rules of quantum mechanics [20]. Also, the transition energy between electron and hole ground states, $\langle e1|E|h1\rangle$, is smaller than that of no-field case, giving rise to the redshift of the absorption edge [20].

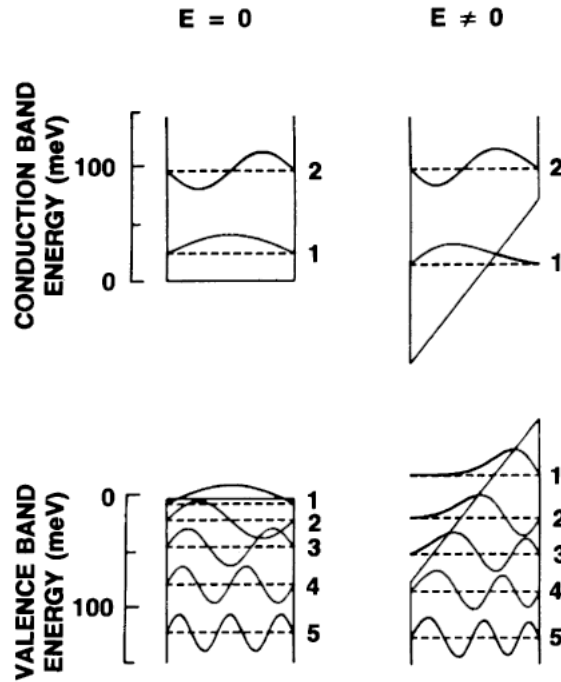


Figure 3.4: Basic concept of quantum confined Stark effect. (After Ref. [14])

A representative measured absorption spectrum for *GaAs/AlGaAs* multiple quantum well (MQW) structure under different external electric field strengths perpendicular to the quantum wells is given in Fig 3.5 [14].

As seen in Fig. 3.5, excitonic peak can clearly be observed for low electric field intensity values, since quantum confinement keeps electron and hole close to each other. This property makes QCSE much more useful for electroabsorption modulation purposes compared to FKE.

QCSE has been widely studied and engineered for related applications in *GaAs* and *InP* platform. Many commercially available high speed quantum electroabsorption modulators, operating in the near infrared (NIR) region that have been widely used in optical telecommunication links [7] and recently demonstrated advanced optoelectronic devices such as wavelength converting crossbar switches [21] utilize QCSE.

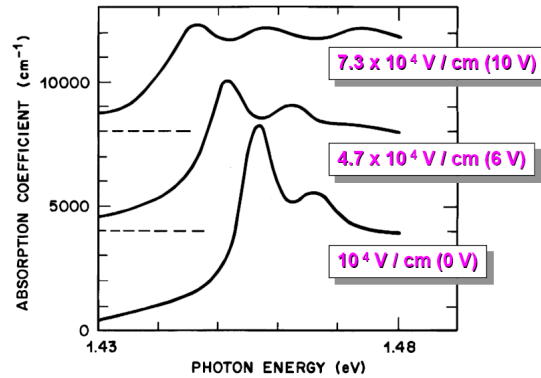


Figure 3.5: Optical absorption spectra for *AlGaAs/GaAs* quantum well structure for various electric fields applied perpendicular to quantum well layers measured at room temperature. The spectra are shifted vertically to dashed levels for clarity. (After Ref. [14])

3.3 Quantum Electroabsorption Modeling

The electroabsorption performance of quantum structures can be analyzed independent of the architecture and electric field application mechanism of the device. Since these quantum structures are very important in the performance of the modulators, it is essential to analyze quantum structure candidates in the design of these devices.

Any quantum structure of finite or infinite quantum well problem can be solved exactly, but only for zero \mathbf{E} field case. Because of this, it is not a preferred way to solve problems analytically when designing EAMs. Instead, numerical methods are used for this purpose. But it is helpful to verify the reliability of a proposed or implemented numerical method, by comparing with the exact solution in simple problems.

There is a number of numerical methods developed to design quantum EAMs of arbitrary potential profiles. Some of these methods are the finite element method (FEM), finite difference method (FDM), Fourier transform method (FTM), and the transfer matrix method (TMM).

These methods are based on the solution of time independent Schrödinger equation (TISE) for the electron (in conduction band) and the hole (in valence band) for semiconductor structures of known material properties. For our purposes TISE excellently

describes electron and hole energy eigenstates [14]¹. Time independent Schrödinger equation is an eigenvalue problem and its solution describes the energy state of carriers for the corresponding potential profile.

Time independent Schrödinger equation for the electron in a quantum well and barrier structure under the electric field \mathbf{E} in z-direction can be expressed as²:

$$\left[-\frac{\hbar^2}{2m_e} \frac{\partial^2}{\partial z_e^2} + V_e(z_e) - e\mathbf{E} \cdot \hat{\mathbf{z}}_e \right] \phi_e(z_e) = E_{nc} \phi_e(z_e) \quad (3.4)$$

Here, in Eq. (3.4), V_e is described by the conduction band potential profile of the quantum structure, m_e is the electron effective mass, ϕ_e is the complex electron wavefunction and E_{nc} is the energy eigenvalue of electron in the reference frame described by V_e .

It is straightforward to write and understand the same equation for holes just by interchanging associated electron terms (coordinate, effective mass, potential and charge) with hole terms as in Eq. (3.5):

$$\left[-\frac{\hbar^2}{2m_h} \frac{\partial^2}{\partial z_h^2} + V_h(z_h) - e\mathbf{E} \cdot \hat{\mathbf{z}}_h \right] \phi_h(z_h) = E_{nv} \phi_h(z_h) \quad (3.5)$$

The resultant electron and hole wavefunctions have discrete energy eigenvalues due to the quantum mechanical essence of the system. By taking the absolute-squared overlap integral of complex electron and hole wavefunctions along the z-axis, one can get a value proportional to probability of finding an electron and a hole in the same vicinity with an energy difference of $E_g + E_{nv} + E_{nc}$. This energy is called the *transition energy* between particular electron and hole states. This information is very useful in predicting the *spectral electroabsorption behavior* of the analyzed quantum structure. Because, each transition that has an energy smaller than particular photon energy adds to absorption rate of such photons by an amount proportional to absolute-squared overlap integral of corresponding electron and hole states.

¹Because electroabsorption mechanisms are much faster (~ 0.1 ps) than the rise/fall time of devices (~ 10 ps).

²under the time evolution of $\exp(-iEt/\hbar)$

Although this way of solving electron and hole energy eigenvalue problem does not take excitonic effects into account by itself, it gives a strong idea about device performance. Also, excitonic effects are introduced as a broadening and a slight redshift of the absorption edge³ according to the value of the overlap integral as long as the excitons are not ionized by internal or external electric fields. For our prospective quantum EAMs, we developed an in-house simulation tool implementing transfer matrix method to be used in our design phase.

3.3.1 Transfer Matrix Method and Its Implementation

Transfer matrix method (TMM), like other methods for the numerical analysis of arbitrary (especially, quantum-confined) structures, formally approximates energy eigenvalues and eigenstates of the structure in question. In the analysis of such an arbitrary potential structure - changing in one direction - we represent it by a step-wise approximation. This reduces the problem of an arbitrary potential to that of a set of many constant potentials obeying appropriate boundary conditions. In such a simple constant potential, the wave is either sinusoidal or exponential. In the formalism of TMM, each of these layers of constant potential have a certain transmission matrix as a function of energy [14], like the ABCD matrix in the analysis of optical components and of two-port electromagnetic networks. For an electron (or hole) having some particular energy, its intensity transmission can be found just by multiplication of these matrices, i.e., cascading each of these layers. For each *quasi-eigenstate*⁴, this probability has a local maxima - in other words, it is resonant with the potential profile.

As depicted in Fig. 3.6, starting with an hypothetical wave (with some particular energy) impinging on one side of the structure, using any maxima finding algorithm (e.g., bisection method), one can iteratively find the *quasi-eigenvalue* along with its associated *quasi-eigenstate*. This way of searching eigenstates is called the *tunneling resonance method* (TRM). The transfer matrix method formalism and the tunneling resonance method are elaborately explained in Appendix A.

³Since Coulomb interaction enhances electron-hole pair generation

⁴not “the eigenstate” due to the numerical nature of the analysis

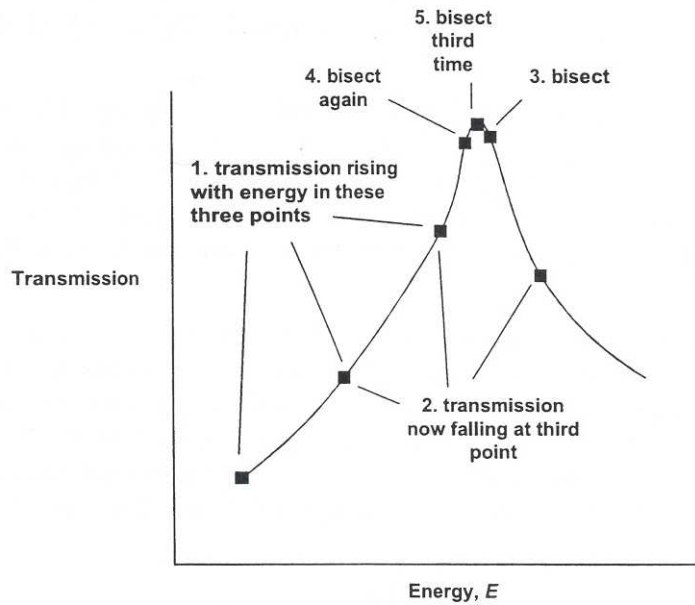


Figure 3.6: Implementation of the tunneling resonance method using bisection method (After Ref. [14]).

We developed and used our simulation tool implementing TMM in a MATLAB[®] installed personal computer (PC) environment.

We started using our in-house simulation tool by checking the reliability of TMM and our implementation. For this, we compared our first simulation results with the results obtained by implementation of other numerical methods and exact solutions for two exactly solvable quantum mechanics problems available in the literature.

Quantum Structure 1

As the first comparison we simulated a single quantum well structure with a barrier height (V_{ba}) of 230 meV and a well width (L_w) of 56 Å. Particle effective mass for the well (m_w) was $0.067m_0$ and for the barrier (m_b) it was $0.0919m_0$, where m_0 is the electron rest mass. For this problem, exact solution gives two bound states with energy eigenvalues of 64.2 and 220.7 meV from the bottom of the well.

For this problem, our and other available results for energy eigenvalues are summarized in Table (3.1). Almost all of the results, including our results, match with the

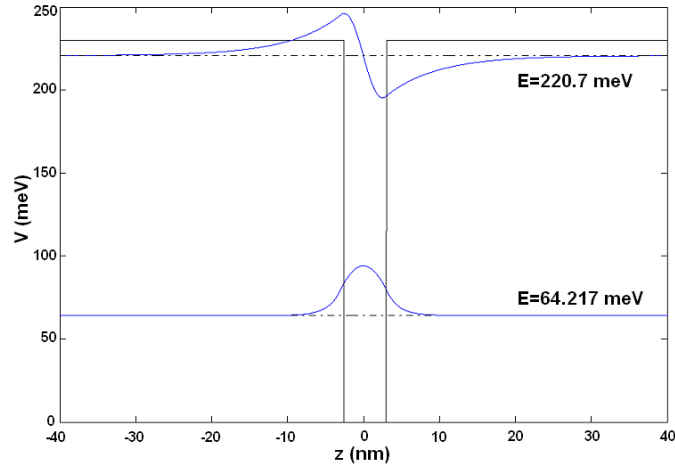


Figure 3.7: Associated energy eigenstates for Quantum Structure 1, obtained by our TMM-based simulation tool.

exact solution (finite difference method [FDM] After Ref. [22] and Fourier transform method [FTM] courtesy of H. V. Demir). Fig. 3.7 shows associated eigenstates and

Table 3.1: Energy eigenvalue results obtained by different methods for Quantum Structure 1.

	Energy states	
	E_1 (meV)	E_2 (meV)
Exact	64.2	220.7
FDM	64.3	220.7
FTM	64.2	220.7
TMM	64.217	220.7

their wavefunctions obtained by our simulation tool.

Quantum Structure 2

It is usually challenging to find *loosely-bound* states for all of numerical techniques in the analysis of quantum-confined structures. To reach the conclusion that our tool works also for loosely bound states, we examined a single quantum well structure with a barrier height (V_{ba}) of 225 meV and a well width (L_w) of 200 Å - for which, exact solution predicts a loosely bound state. Particle effective mass for the well (m_w) was $0.067m_0$ and for the barrier (m_b) it was $0.0919m_0$, where, again, m_0 is the electron rest mass. For this problem exact solution gives five eigenstates, the fifth state

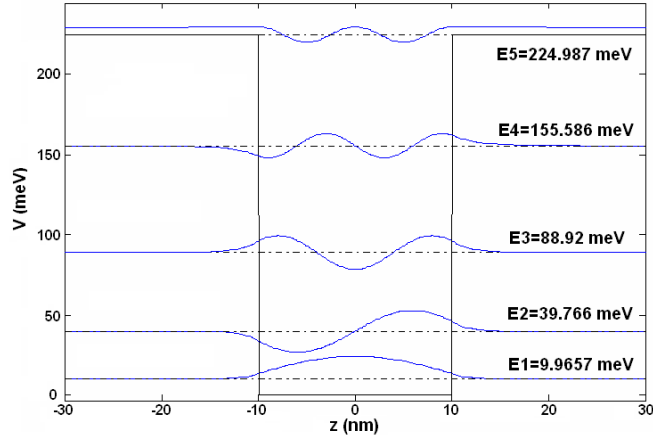


Figure 3.8: Associated energy eigenstates for quantum structure 2, obtained by our TMM based simulation tool.

being a loosely-bound one. The results are summarized in Table (3.2) (finite element method [FEM] After Ref. [23], and Fourier transform method [FTM], courtesy of H.V. Demir). Fig. 3.8 shows associated eigenstates (including the loosely bound state)

Table 3.2: Energy eigenvalue results obtained by different methods for quantum structure 2

	Energy states				
	E_1 (meV)	E_2 (meV)	E_3 (meV)	E_4 (meV)	E_5 (meV)
Exact	9.97	39.77	88.92	155.58	224.99
FEM	9.97	39.77	88.93	155.59	Not Found
FTM	9.97	39.77	88.92	155.57	224.9
TMM	9.9657	39.766	88.92	155.586	224.987

and their wavefunctions obtained by our simulation tool. Our results showed that our TMM-based simulation tool successfully works and that we can use it in the design and analysis of any arbitrary potential profile (including those made of *GaN* based material system).

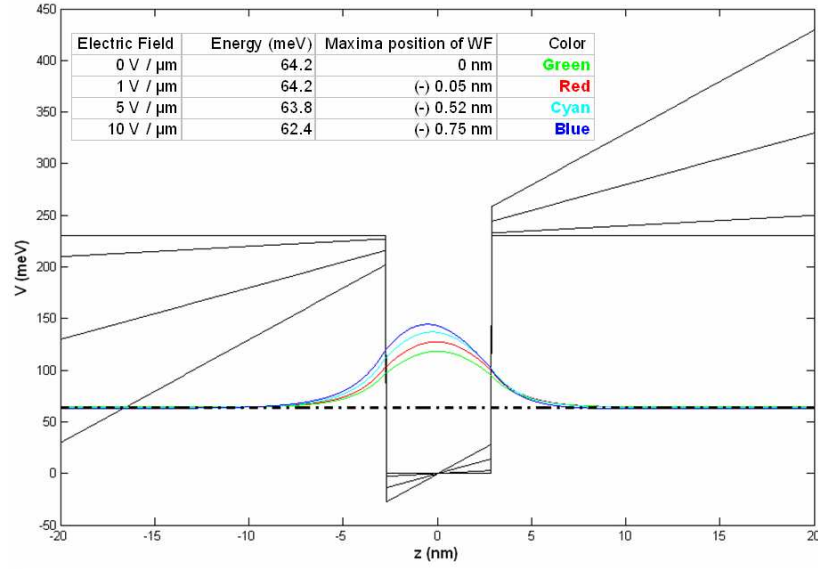


Figure 3.9: Associated electron eigenstates and energy eigenvalues for $Al_{0.3}Ga_{0.7}As/GaAs$ quantum structure obtained by our TMM based simulation tool (wavefunctions are normalized to different values for visualization purposes).

3.3.2 Theoretical Demonstration of Quantum Confined Stark Effect Using Transfer Matrix Method

Using our simulation tool, we can also demonstrate quantum confined Stark effect. We computed the electron and hole states of a $GaAs/Al_{0.3}Ga_{0.7}As$ single quantum well structure for different external electric field intensity levels. For the electron states we obtained the wavefunction and energy eigenvalues as summarized in Fig. 3.9 (here note that no broadening is used). As depicted in this figure, the energy eigenvalue of the electron decreases and electron wavefunction moves under the effect of the external field as the field is increased. In agreement with the QCSE mechanism.

The resulting absorption spectrum we obtained is shown in Fig. 3.10. This figure shows that we can successfully demonstrate QCSE with its redshift with increasing electric field in our simulation environment and model quantum electroabsorption in semiconductor quantum structures.

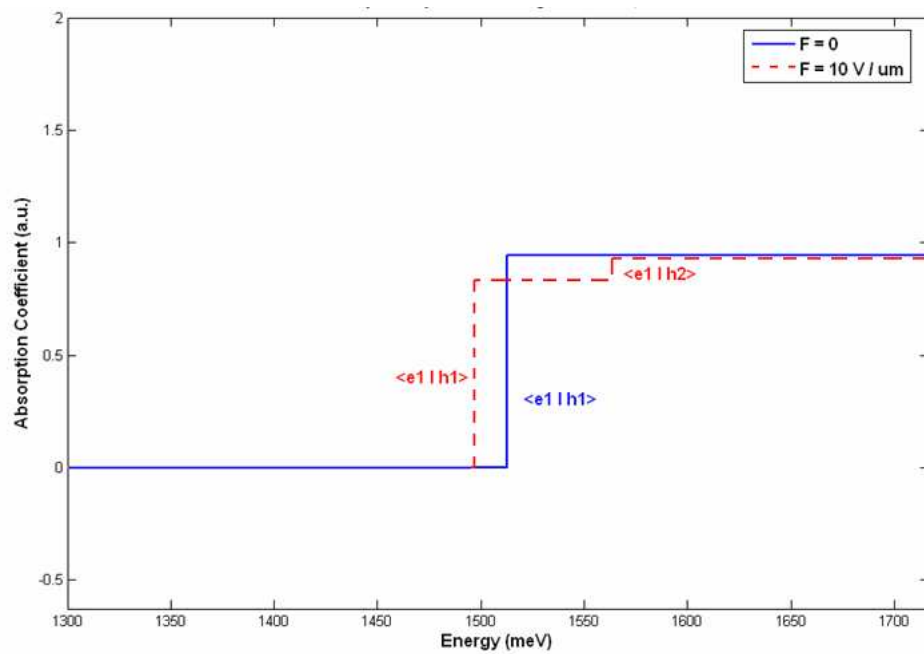


Figure 3.10: Absorption spectra for $Al_{0.3}Ga_{0.7}As/GaAs$ quantum structure for different external electric field intensities obtained by our TMM based simulation tool.

Chapter 4

DEVICE IMPLEMENTATION

This chapter summarizes our main device implementation on III-nitride device platform, describing our design approach, material growth, device fabrication, and characterization step by step.

4.1 Design Work

Our design work consists of three parts: Quantum design in which we design the quantum structures, the epitaxial design in which we design the set of epitaxial layers according to the quantum design and device consideration and finally the device design in which we design the architecture of our devices.

4.1.1 Quantum Design

In our quantum design part, we basically simulate possible quantum structures for their utilization in electroabsorption. We compute the electron and hole energy eigenvalues and wavefunctions using TMM based simulation tool with appropriate material parameters. We then calculate their absolute-squared overlap integrals for different levels of external electric fields as we did for *AlGaAs/GaAs* quantum structures. For

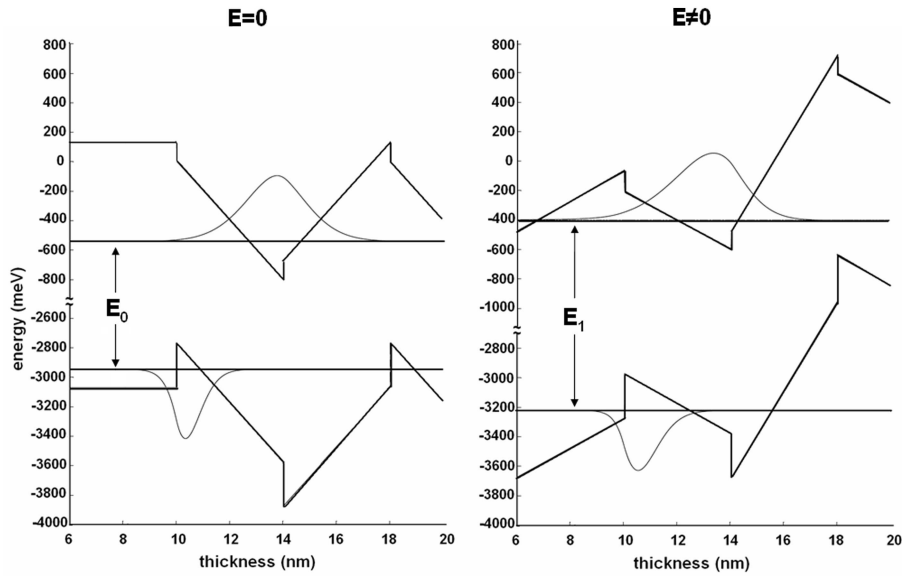


Figure 4.1: Wavefunctions of $In_{0.1}Ga_{0.9}N/GaN$ quantum structures that we calculate using TMM for zero and non-zero external electric field cases.

a desired wavelength of operation (e.g., 400 nm) we obtain the predicted absorption spectra and so the change in absorption level with the external electric field.

As a quantum structure to be examined, we can simulate an $In_{0.1}Ga_{0.9}N/GaN$ multiple quantum well structure that consists of 5 quantum wells and barriers each being 4 nm thick. The band diagrams for zero and non-zero external field cases and the electron and hole wavefunctions we computed according to them are shown in Fig. 4.1.

In Fig. 4.1 we theoretically show that absorption edge shifts to larger photon energies, and thus shorter wavelengths, as the external field intensity is increased since the external electric field is in opposite direction to the built-in electric field inside the wells. This behavior (blueshift) is opposite to the conventional QCSE. We shall also show and verify this extraordinary behavior experimentally later in this chapter.

As mentioned earlier, we can obtain calculated absorption spectra using overlap integrals for various external electric field intensities. In Fig. 4.2 we show the predicted absorption spectra for various external electric field intensity levels. Again, we can see that absorption edge shifts to shorter wavelengths. The magnitude of relative absorption level change is also important in this step, which seems to be good for the

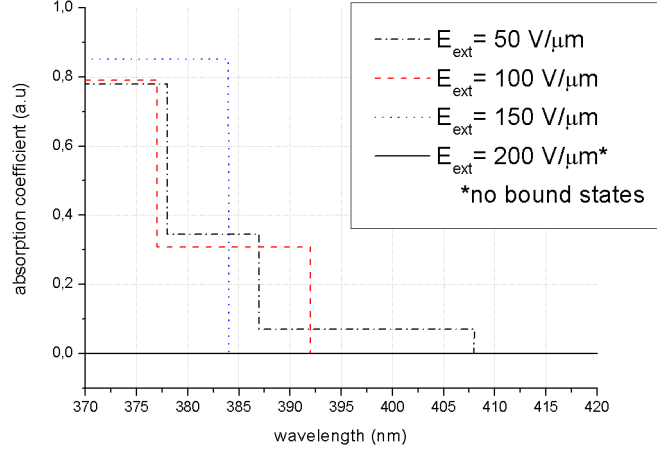


Figure 4.2: Absorption spectra for $In_{0.1}Ga_{0.1}N/GaN$ quantum structures that we calculate using TMM.

design in Fig. 4.2. Having made sure that absorption level change is adequate, we finalize the decision about well and barrier materials and their thickness for our device active layer. Using our TMM-based simulation tool, we examined various quantum structures and determine the expected strength of quantum confined Stark effect.

Excitonic Effects in III-Nitride Quantum Heterostructures

As mentioned in the quantum confined Stark effect section, excitons are of special importance for the utilization of this effect. In principle, strength of excitonic effects can be related to overlap integral of electron and hole wavefunctions. For polar III-nitride quantum structures, however, excitons are usually ionized because of the built-in polarization induced electrostatic fields inside the well structure. In the design part, our simulation results show that when this field is compensated by the external electric field electron and hole move towards each other, enhancing excitonic effects. However, in the real case it is not usually possible to get such abrupt heterojunctions as we model in our simulations. Also, external electric field has the same direction as the polarization-induced barrier field. Because of these two, electrons and/or holes tend to tunnel out of the structure easier than we expect in our simulations. This tunneling causes the diminishing of excitonic effects. In agreement with this argument, we

can find no bound states when we increase the external electric field further in our simulations. So both polarization-induced electrostatic fields in the well and barrier structures and external electric field are against the excitonic effects. Under this trade-off, and remembering the dependence of well and barrier fields on the well-to-barrier width ratio ($d_{barrier}/d_{well}$), an optimal operating range would be about 1 for excitonic effects to take place strongly. We shall re discuss these effects for our structures under the experimental results later in this chapter.

4.1.2 Epitaxial Design

In the epitaxial design, we determine the alloy content and thickness of all the layers. Our designs were based on a p-i-n diode structure with p- and n-layers that are transparent at the operation wavelength. In order to prevent undesired reactions between metalorganic vapors and ammonia (which cause cracks) and initiate crystallinity, we include a low temperature grown GaN or AlN nucleation layer in the beginning of the growth [24], which are also transparent at the operation wavelength. In order to obtain a high crystal quality, we introduce thick (typically 200 nm) GaN buffer layer after the nucleation layer. A typical epitaxial design is given Table (4.1).

Table 4.1: A representative epitaxial design.

No.	Name	Thickness	Doping	Loop
8	p-type <i>GaN</i> contact layer	120 nm	Mg (max)	1
7	p-type $Al_{0.1}Ga_{0.9}N$	10 nm	Mg (max)	1
6	<i>GaN</i> barrier	4 nm	uid.	1
5	$In_{0.1}Ga_{0.9}N$ well	4 nm	uid.	5 (with layer 4)
4	<i>GaN</i> barrier	4 nm	uid.	5 (with layer 5)
3	n-type <i>GaN</i> contact layer	700 nm	Si (max)	1
2	High Temp. <i>GaN</i> Buffer	200 nm	undoped	1
1	Low Temp. <i>GaN</i> Nucleation	14 nm	undoped	1
0	c-plane sapphire			

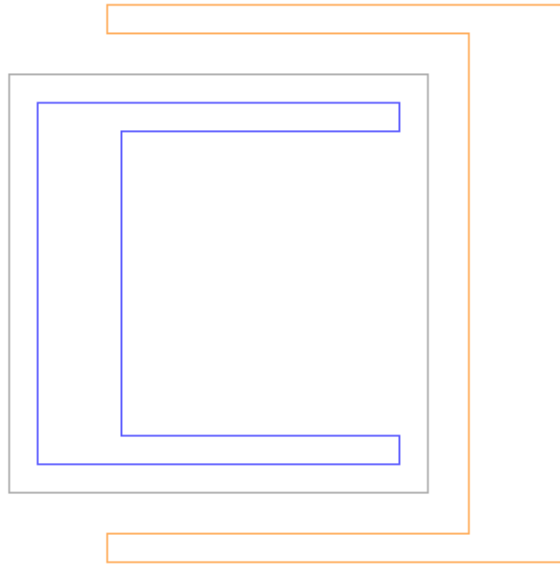


Figure 4.3: Layout program view of a modulator in our photomask design.

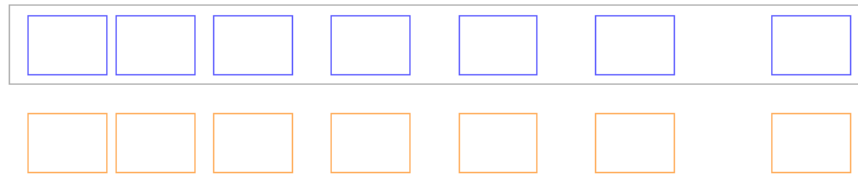


Figure 4.4: Layout program view of TLM grids in our photomask design.

4.1.3 Device Design

The device design part consists of photomask layout design for microfabrication. We designed our devices to be surface-normal, having a mesa (table-top shape) architecture. The devices to be characterized should have open or at least semi-transparent optical windows to be tested for their electroabsorption performances. The mesa sizes vary between $300 \mu m \times 300 \mu m$ and $10 \mu m \times 10 \mu m$. A typical size of a chip can be $6mm \times 6mm$. The photomask includes as many devices as possible. We also designed TLM (transmission line method) grids to determine ohmic contact parasitic resistance of the devices and the resistivity of epitaxial structures. In Figs 4.4 and 4.3 are shown the layout program view of one of the $300 \mu m$ mesa modulators and the TLM grids, respectively.

We use the same photomask for all our epitaxial structures. Having completed all the design steps, we begin our experimental work.

4.2 Experimental Work

In this section, we explain our experimental work: growth, fabrication and characterization. As mentioned earlier, we have grown all of our wafers on c-plane sapphire substrates using MOCVD. Device microfabrication and characterization processes were completed at class-100 and class-10.000 environments of Bilkent University Advanced Research Laboratory of the Physics Department and Nanotechnology Research Center (NANOTAM).

4.2.1 Growth

Mainly one MOCVD system was used for the growth of our modulator wafers at Bilkent NANOTAM. For the growths, we use TEGa (for quantum structures), TMIn, TMGa, TMAI and NH_3 as semiconductor precursors. For n- and p-type dopant precursors, we use SiH_4 and Cp_2Mg , respectively. As mentioned earlier, we need a low growth rate in the growth of quantum structures. For this purpose, as suggested in the literature, we used TEGa and a low III-V flow molar ratio [25].

The MOCVD at Bilkent NANOTAM uses LayTec EpiR reflectivity system, which simultaneously measures reflectivity at different wavelengths as an in-situ measurement tool. A full oscillation in reflectivity-time chart relates to the thickness of material grown within that time interval via the wavelength and refractive index of the material. This enables us to monitor the thickness of grown material and determine the growth rate. The strength of reflectivity signal is also correlated with the crystal quality and this gives us the chance to control and improve crystal quality during the growth. In Fig. 4.5 is given the reflectivity measurement results of a successfully

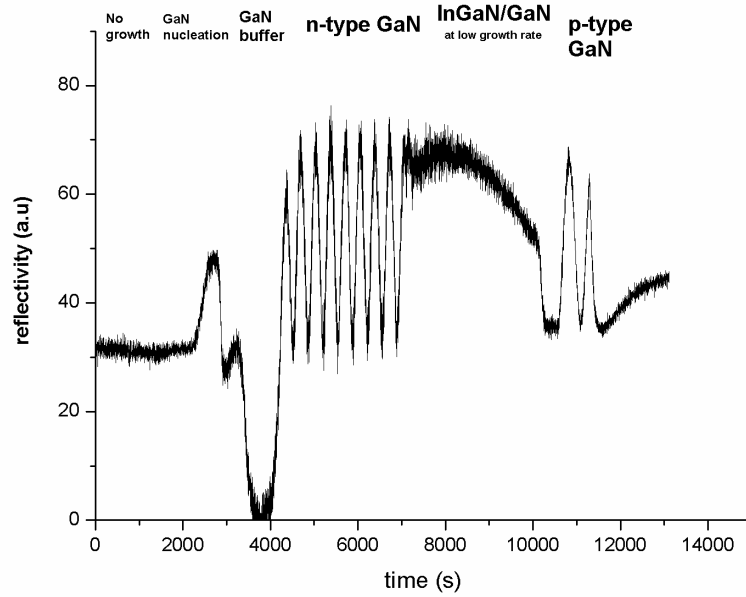


Figure 4.5: In-situ reflectivity measurement results for *InGaN/GaN* quantum electroabsorption modulator wafer at $\lambda=541.4$ nm where the wafer is transparent.

grown *InGaN/GaN* quantum modulator wafer. Grown material in each time interval is indicated on this figure.

4.2.2 Material Characterization

For the best quantum EAM operation, the grown material should meet some certain specifications such as a strong photoluminescence peak at room temperature and an RMS (root-mean-square) surface roughness of a reasonable value. When we make sure that the grown material meets these specifications, we fabricate and test the devices.

Our material characterization steps consists of atomic force microscopy (AFM) analysis for surface roughness; photoluminescence (PL) measurement for the determination and quality of quantum structures; transmission measurement for bandgap determination of the bulk layer that has the widest bandgap, and secondary ion mass spectrometry (SIMS) measurement¹ for the verification of materials in each layer.

¹We outsource this measurement as a service from a material analysis company (HIDEN Analytical) located in the UK.

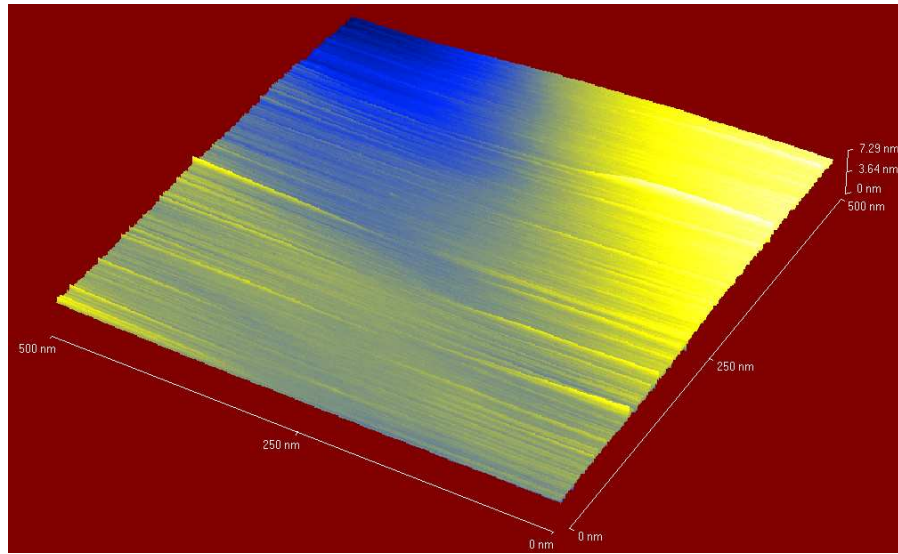


Figure 4.6: $0.5 \mu\text{m} \times 0.5 \mu\text{m}$ atomic force microscope image taken from one of our wafers.

Fig. 4.6 shows the contact-mode AFM scan results of the wafer with the roughest surface among all our successfully grown wafers. It has 0.85 nm RMS surface roughness which is a reasonable value for our purposes.

Fig. 4.7 shows the room temperature photoluminescence (PL) spectrum obtained by our PL setup that includes a He-Cd laser with an excitation wavelength of 325 nm , and a monochromator. We observe the PL peak at 430 nm with a full width at half maximum (FWHM) of 14 nm for a 5 InGaN/GaN quantum well barrier structure. In the PL spectrum, we see both GaN (bulk) and InGaN/GaN quantum photoluminescence, latter being stronger.

In Fig. 4.8, we see the wafer transmission spectrum obtained by a pulsed Xe light source and a spectrometer. Since the bulk layer with the widest bandgap material is GaN for this structure, we see GaN absorption edge, which is at around 360 nm .

In the SIMS depth profile of one of our wafers with 15 InGaN/GaN ($4 \text{ nm}/4 \text{ nm}$) quantum structures protected by a thin p-AlGaIn layer, we see p- and i- layers. Quantum structures cannot be resolved clearly due to erosion effects, however total thickness of the active layer is approximately as we expected by our growth rate calculations.

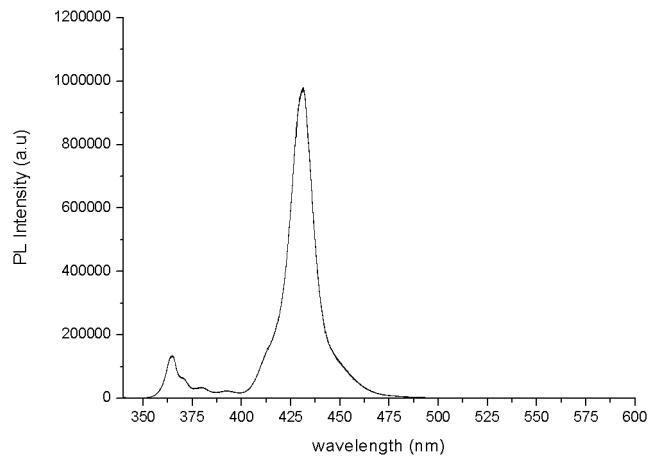


Figure 4.7: Photoluminescence spectrum of one of our epi-wafers

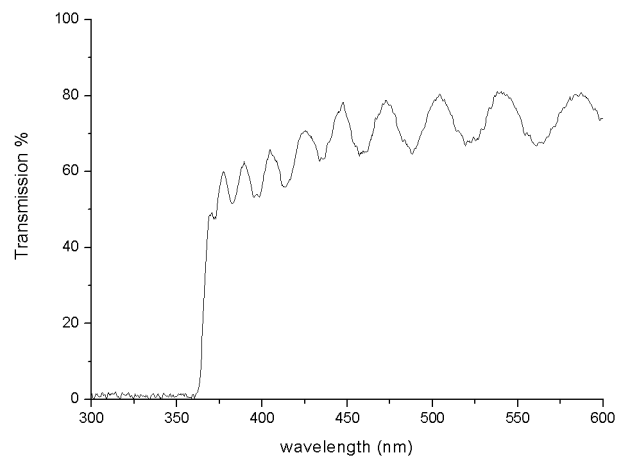


Figure 4.8: A typical wafer transmission spectrum for our *InGaN/GaN* quantum electroabsorption modulators.

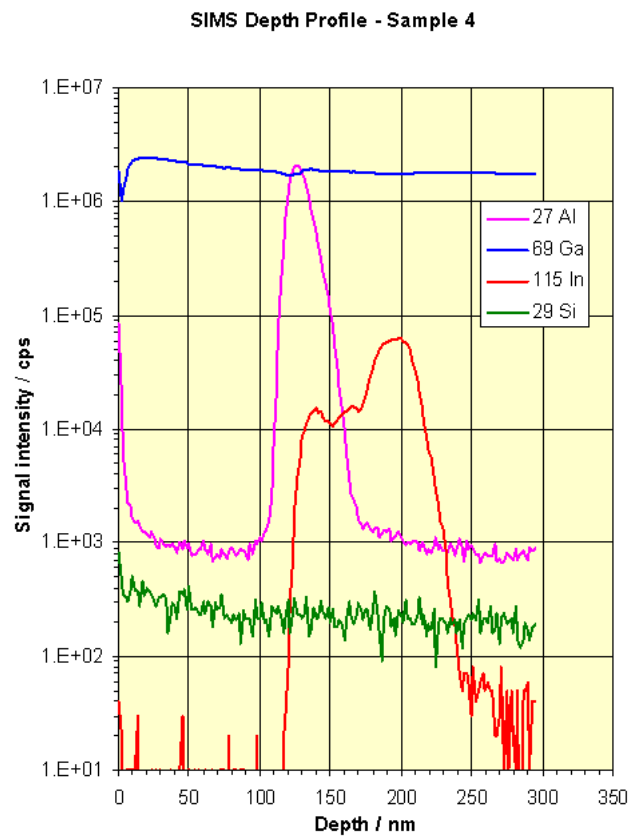


Figure 4.9: SIMS analysis results of one of our wafers with 15 *InGaN/GaN* quantum well/barrier structures.

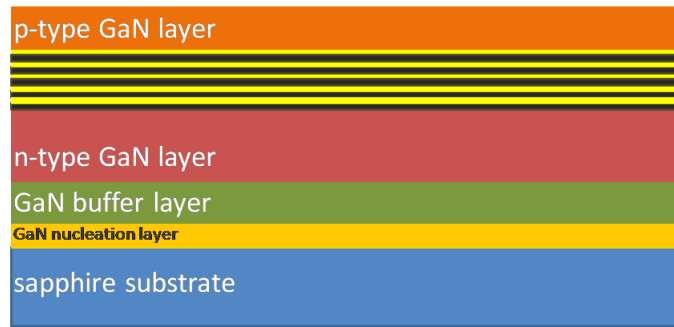


Figure 4.10: Device after cleaning.

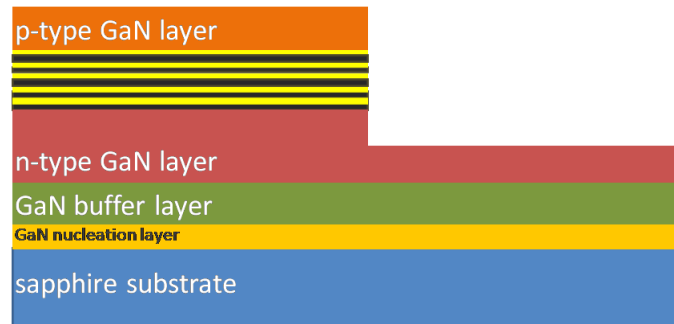


Figure 4.11: Device after mesa etching.

4.2.3 Fabrication

Microfabrication process was completed in the class-100 environment of the Advanced Research Laboratory (ARL). Our fabrication started with activation of Mg dopants by keeping the whole wafer at 750°C in a nitrogen ambient. We then cleaved the chips from the backside of the wafer as a square about one centimeter on one side, according to our photomask design. After a cleaning process that consists of ultrasonic bath in acetone and then isopropanol, each being 5 minutes, we dried the sample with a pressured nitrogen gas. We applied positive photolithography (removal of UV exposed photoresist via developer) for the definition of p-mesas and use reactive ion etching (RIE) with Freon-12 (CCl_2F_2) plasma to land at n-type semiconductor layer.

Subsequently, we again used positive photolithography for p-contact features. We evaporated Ni/Au (10/100 nm thick) for p-contact metallization. We used nickel for the adhesion of gold to p-type *GaN*. We then applied a lift-off process to remove metals that have photoresist underneath.

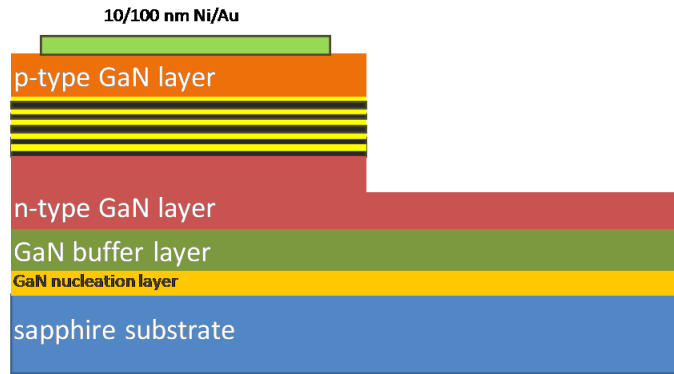


Figure 4.12: Device after p-contact formation.

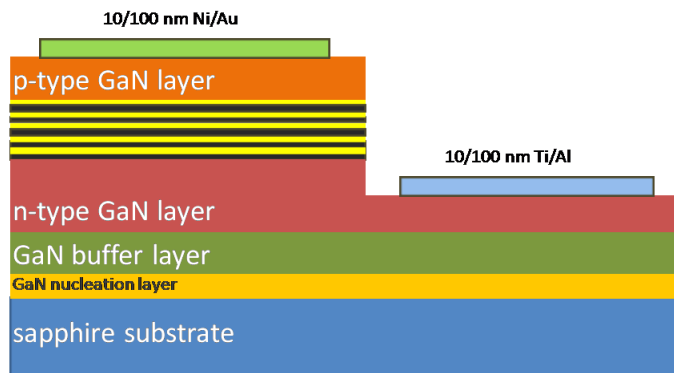


Figure 4.13: Device after n-contact formation and annealing.

For n-contacts, we again define the contacts via positive photolithography and evaporated Ti/Al (10/100 nm thick). After the n-contact lift off, we applied rapid thermal annealing for alloy formation in the metal-semiconductor interface to get ohmic contacts instead of Schottky contacts. We annealed our samples at 600°C typically for 1 minute in a nitrogen ambient. Fig. 4.14 shows a micrograph of one of the modulators we fabricated at Bilkent University.

4.2.4 Device Characterization

Our device characterization steps include electrical and optoelectronic characterization techniques. We measured the current-voltage (IV) characteristics of our devices. Since all are p-i-n diodes, they have a diode type of rectifying IV characteristics as shown in Fig. 4.15. Turn on voltage is typically about 2.5 Volts. In forward bias, we obtained electroluminescence (EL) out of our devices, with a spectrum shown in Fig. 4.16 for a

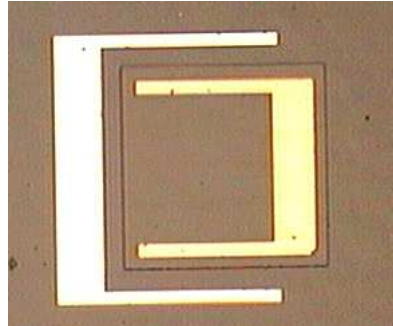


Figure 4.14: Micrograph of a fabricated device.

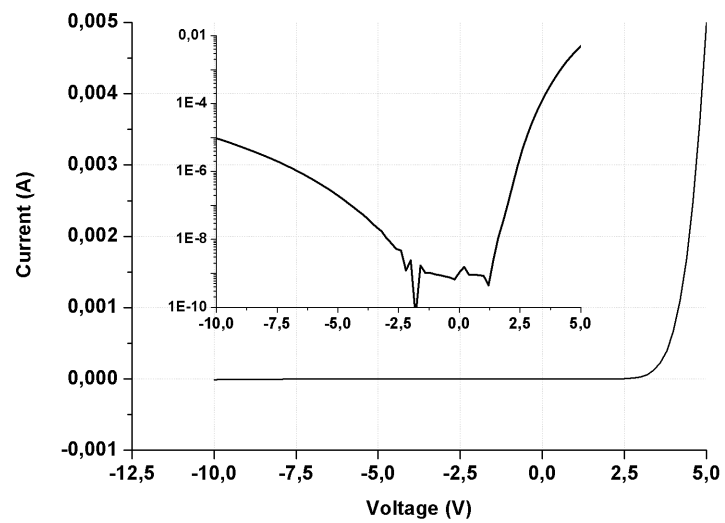


Figure 4.15: IV curve of one of our modulators, inset shows the semilog scale IV characteristics.

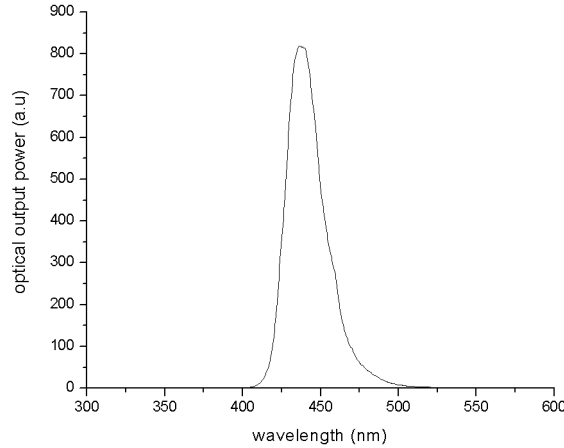


Figure 4.16: Electroluminescence spectrum of one of our modulators.

device with 4 nm/4 nm *InGaN/GaN* quantum structures [26] [27]. The narrow width (full width at half maximum $\sim 60\text{nm}$) of EL spectrum reveals the growth of quantum structures of similar properties.

We measured the optical absorption spectra using our photocurrent measurement setup that includes a monochromator, a xenon (Xe) lamp, a lock-in amplifier, an optical powermeter, chopper and a dc power supply for the application of various reverse bias voltages. A diagram showing the the setup is given in Fig. 4.17. We control spectral optical power coming from the xenon lamp spectrally using the monochromator and the optical powermeter. By using Eq. (3.3) (the formula that relates photocurrent to absorption coefficient), we obtained the absorption spectrum for each voltage level. Fig. 4.18 shows the optical absorption spectra for a device having 5 *InGaN/GaN* quantum structures. The spectra span a wavelength range from 400 to 460 nm and are parameterized with the applied reverse biases from 0 to 6 V, with the dark current levels in the range of few nanoamperes. Here, in agreement with our simulations, we observe that the optical absorption edge blueshifts with the increasing applied reverse field, unlike in the case of the conventional QCSE. Because of this, we call this reversed quantum confined Stark effect (RQCSE) [26]. Inset of Fig. 4.18 shows the 0 V absorption curve, exhibiting an excitonic shoulder around 420 nm.

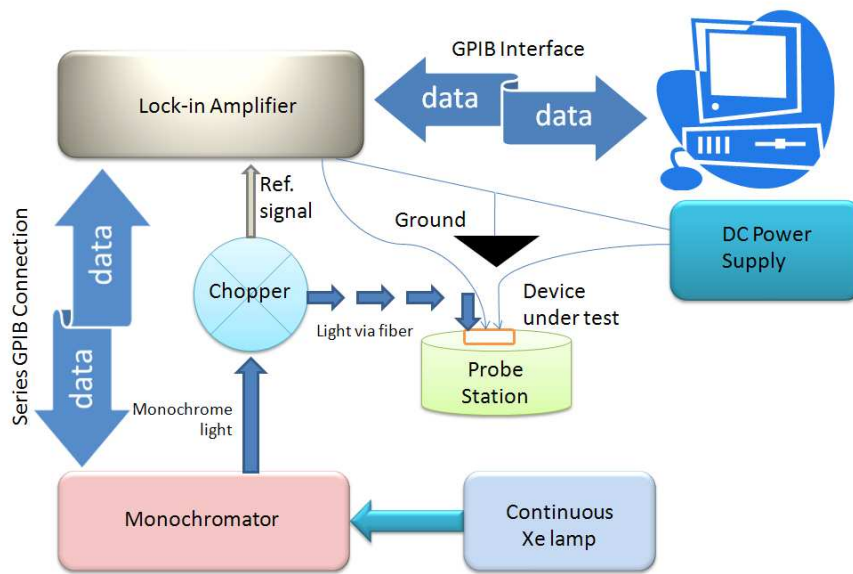


Figure 4.17: Electroabsorption test setup.

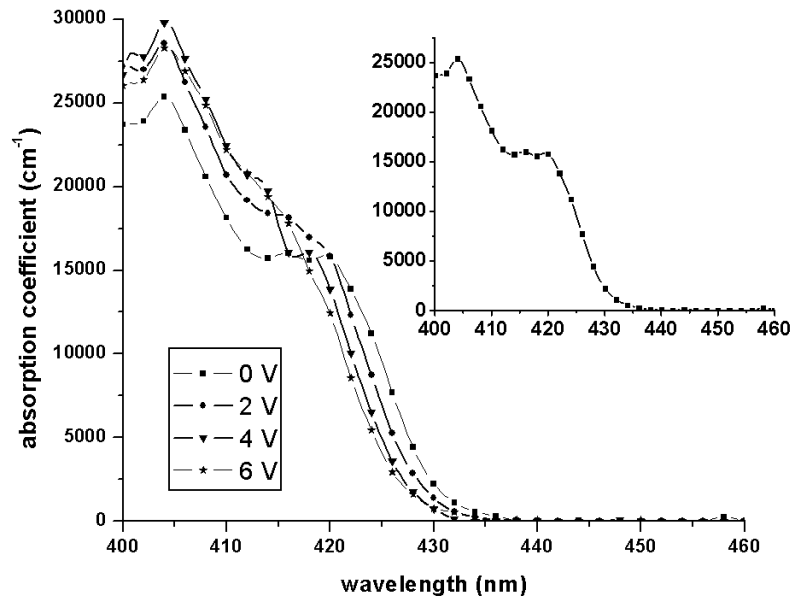


Figure 4.18: Electroabsorption spectra of 4 nm/4 nm *InGaN/GaN* quantum modulators. Inset shows the 0 V absorption curve separately.

This blueshift is a direct experimental evidence of the polarization induced electrostatic fields seen in the wells in the opposite direction of the applied reverse field, thus in the opposite direction of the built-in field. Therefore, the well polarization field lies in the opposite direction of the epi-growth and extends from the top epitaxial layer (p side) toward the bottom epitaxial layer (n side), verifying the expected direction of the polarization in the *InGaN* wells on polar c plane. Also, in Fig. 4.18, we observe an inflection point at 418 nm on the absorption curves of our *InGaN/GaN* quantum structures under different biases, which is in agreement with the previous work of Friel et. al. [28] on *GaN/AlGaN* quantum structures.

In Fig. 4.19 is shown the absorption coefficient change (with respect to the 0 V absorption level) with the largest change of 6000 cm^{-1} for a 6 V swing (corresponding to 50 cm^{-1} absorption coefficient change for $1 \text{ V}/\mu\text{m}$ field change) at 424 nm. This absorption coefficient change is the largest ever reported in this wavelength range compared to previous work of Kneissl et. al. with $<5000 \text{ cm}^{-1}$ for 7.2 V swing [29].

As seen in Fig. 4.19, this device is optimal for the blue region between 420 nm and 430 nm with large absorption change and low background absorption ($\sim 767 \text{ cm}^{-1}$). In Fig. 4.19, we also show the optical transmission spectra modulated with the reverse bias in the inset. The transmission and absorption spectra lead to the same observations of the blueshift and inflection point at 418 nm. Here, in the surface-normal configuration, the short optical interaction length of 50 nm, along with % 17 stray light not passing through the mesa, renders a low transmission modulation of 3.05 % at 424 nm for 5 V reverse bias, as also expected by the absorption spectra.

By operating our device at low forward bias voltage levels that are smaller than the built-in potential (V_b) (and thus still operating the device effectively under the net reverse field), we also measured electroabsorption to understand the underlying physics better. Due to the determined direction of polarization fields, we observe traditional QCSE in effect in the case of forward bias as given in Fig. 4.20. This experimental demonstration shows us that it is possible to blue-shift or red-shift the same polar quantum structure depending on the direction of applied electric field (either in the opposite or the same direction of the polarization induced built-in electrostatic fields

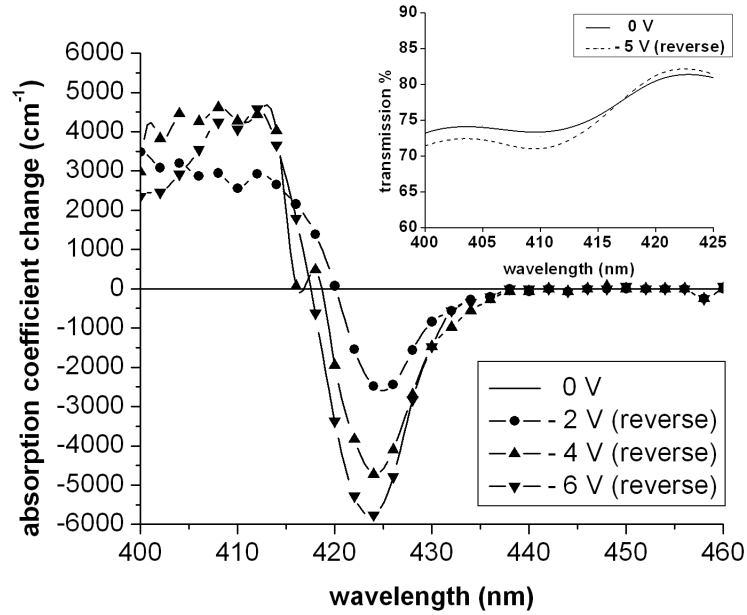


Figure 4.19: Absorption coefficient change with respect to 0 V absorption. Inset shows the transmission spectrum for 0 and 5 V reverse bias.

seen in the wells, respectively). To best of our knowledge, this is the first demonstration of electric field direction dependent electroabsorption behavior change (i.e., blueshift with external electric field in one direction, redshift with external electric field in the other direction) ever reported [26]. In quantum well structures, QCSE exhibits redshift regardless of the direction of applied field; here we demonstrate that this is not the case for polar zig-zag quantum structures, where square-well condition is broken with the polarization induced built-in electrostatic fields.

Excitonic Effects in III-Nitride Quantum Heterostructures Revisited

For the understanding of this reversed electrobabsorption behavior better and for investigating our optimal well-to-barrier thickness ratio argument, we explored the dependence of this ratio on excitonic effects. In order so doing, we grew and fabricated an *InGaN/GaN* modulator of 5 well 2.5 nm/7.5 nm structure as a collaborative research effort between Bilkent University and Chonbuk National University of Korea. At Bilkent, we fabricated these devices and compared to our 4 nm/4 nm quantum

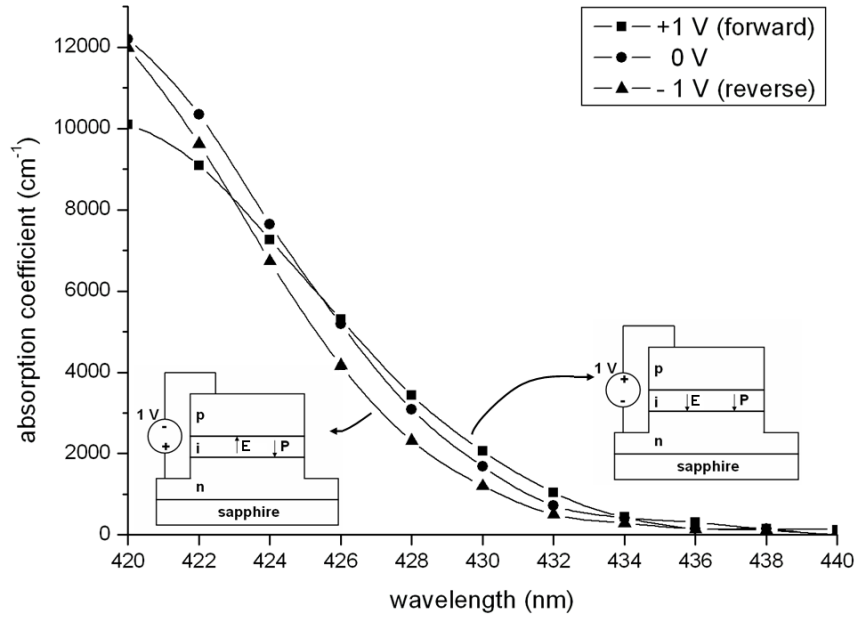


Figure 4.20: Field direction dependent demonstration of reversed and traditional quantum confined Stark effect. E denotes the external electric field and P denotes the polarization-induced electrostatic field inside the quantum well.

structure. In agreement with our previous argument, we observe a poorer electroabsorption behavior compared to devices of 4 nm/4 nm well/barrier thickness [30] as given in Fig. 4.21. However, as again expected, we still observe the reversed quantum confined Stark effect [30].

Tunability

For our devices we also explored tunability in order to get electroabsorption and reverse quantum confined Stark effect for different wavelengths. We also demonstrated these effects for a device to operate at 485 nm as a joint research effort between Bilkent University and Chonbuk National University in Jeonbuk, South Korea [30]. Again, we observe the reversed quantum confined Stark effect for this structure. The electroabsorption spectra for this device is given in Fig. 4.23.

Since this requires more InN incorporation to quantum well structures, it is difficult to grow high quality *InGaN* quantum layers without having thicker (8 nm) GaN quantum barrier structures. For the achievement of 485 nm operation we sacrifice the

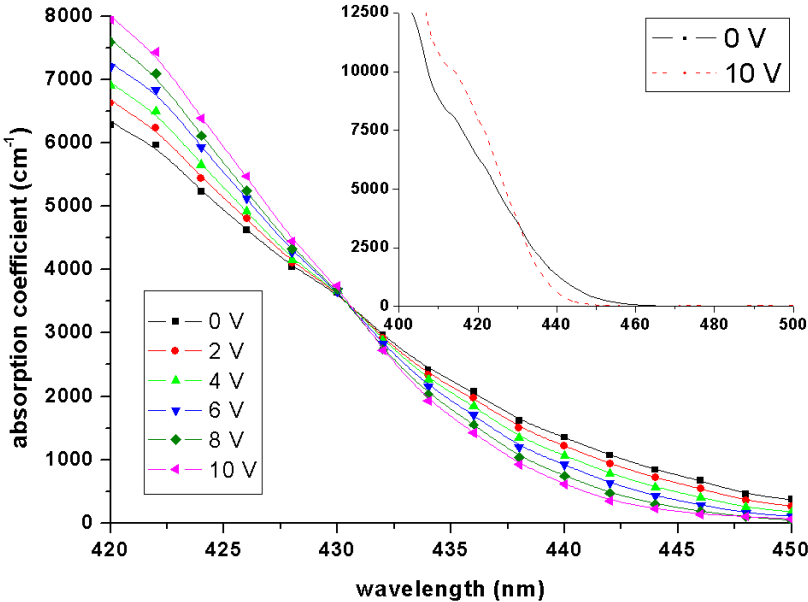


Figure 4.21: Electroabsorption spectra of 2.5 nm/7.5 nm *InGaN/GaN* heterostructure. Inset shows the 0 V and 10 V absorption curves separately.

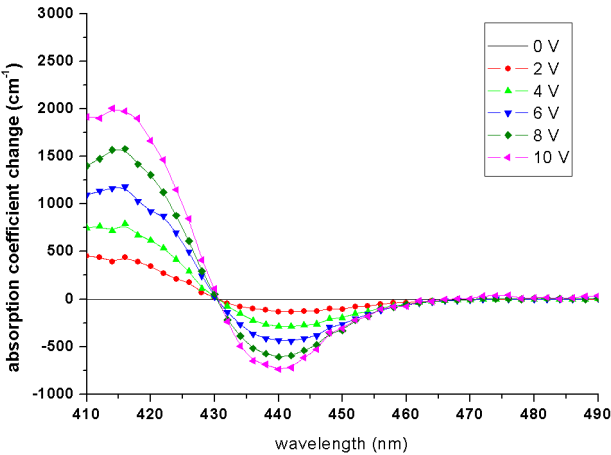


Figure 4.22: Absorption coefficient change with respect to 0 V absorption for the device of 2.5 nm/7.5 nm quantum structure. Inset shows the 0 V and 10 V absorption curves separately.

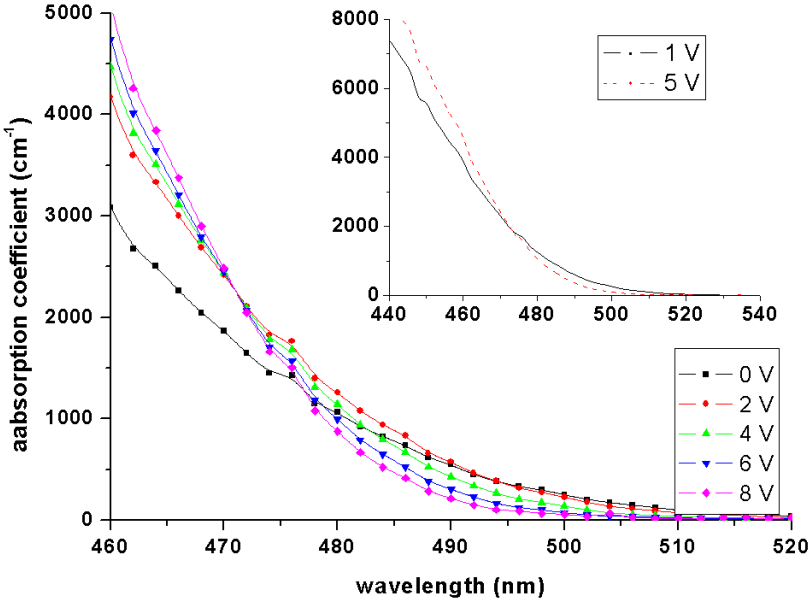


Figure 4.23: Electroabsorption spectra of the device that operates 485 nm for various reverse bias voltage levels. Inset shows the same of 1 V and 5 V bias in a wider spectrum showing a low level of excitonic effects.

thinness of active layer, so absorption coefficient change is lower for these structures as given in Fig. 4.24. Again, by both increasing the mismatch between well and barrier layers and increasing the barrier width, we obtain a poorer excitonic behavior.

Also, since built-in polarization induced electrostatic field strength increases with the mismatch between well and barrier layers, we observe a poorer excitonic behavior and absorption coefficient change.

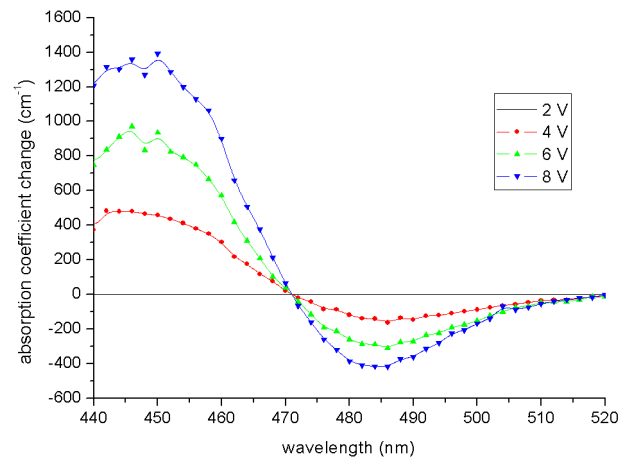


Figure 4.24: Absorption coefficient change with respect to 2 V absorption for the device optimized for 485 nm wavelength of operation.

Chapter 5

CONCLUSIONS AND FUTURE DIRECTIONS

5.1 Conclusions

In this thesis work we demonstrated reversed quantum confined Stark effect both theoretically and experimentally for *InGaN/GaN* quantum structures. We showed that we control the device performance and operating wavelength by engineering quantum structures with our designs. By tuning the InN concentration in the quantum well structures, we showed that can tune the operation wavelength from blue to green. We also showed that this approach provides solutions for certain applications that require electroabsorption at different wavelengths of operation. Also, by obtaining an optimal well-to-barrier width ratio with our quantum designs, we demonstrated the largest electroabsorption with our modulators and broke a world record the the blue wavelength range of operation. Moreover, to best of our knowledge, for the first time we demonstrated a field-direction dependent quantum electroabsorption behavior in semiconductor quantum structures.

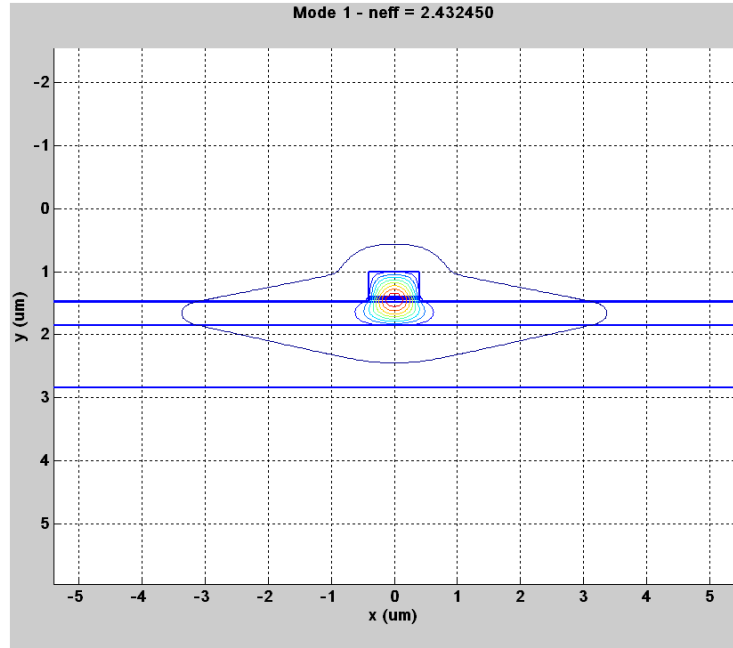


Figure 5.1: Dominant mode E-field profile for one of our rib waveguide designs (in collaboration with M. Yorulmaz of our group).

5.2 Future Directions

As mentioned earlier, contrast ratio of an electroabsorption modulator can be increased by increasing the optical interaction length using waveguide structures. Waveguide modulators are, in fact, very similar to edge emitting laser diodes. We need the dominant mode to interact with the active layers (gain medium for laser diodes and electroabsorption modulators) as much as possible, quantified with the Γ confinement factor. So one has to carefully design the waveguide for this purpose. We initiated a theoretical research effort on the design of such waveguides. Fig. 5.1 shows one of the rib waveguides we designed along with its dominant mode E-field profile.

However it is not straightforward to fabricate such waveguides with desired properties. Similar to edge emitting laser diodes, for waveguide modulators one needs preferably mirror-like facets. Crystallographic cleaving (which is the most popular method for *GaAs/InP* based laser diode and waveguide modulator fabrication) cannot be applied to *GaN*-on-sapphire structures. Dry etching, on the other hand, causes saw-like edges on the etched surface as shown in scanning electron micrograph obliquely taken from a *GaN* based device in Fig. 5.2. An additional crystallographic smoothing step,

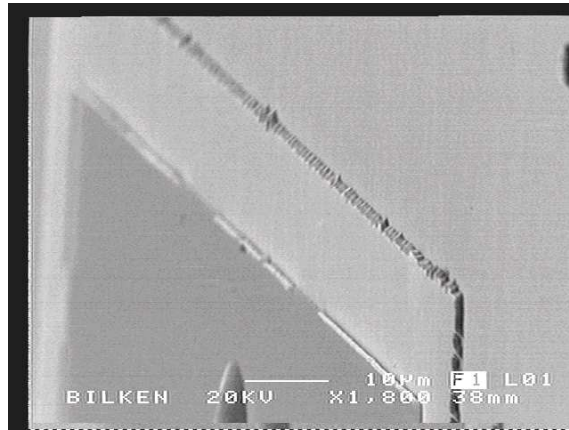


Figure 5.2: Scanning electron micrograph obliquely taken from one of our devices (etched in RIE).

called photoelectrochemical (PEC) etching can be performed for this purpose. Having obtained good results as absorption coefficient change and low background absorption, we will continue with utilizing this method in order to improve the contrast ratio of our modulators and further study the transient response of our modulators as the modulation frequency is increased.

Moreover, it is important that we have electroluminescence from our devices. For an even more compact solution of optical clocking in the blue, a laser diode-waveguide modulator integration on the same chip can be considered. However, there are difficulties related to setting the modulation and emission on the same wavelength and the fabrication issues. We will address these challenges in our future research.

APPENDIX A

TRANSFER MATRIX METHOD

In the transfer matrix method formalism that we adapt from Prof. D. A. B. Miller of Stanford University, [14] we model the actual, continuously-varying (in one direction) potential profile by a discrete and step-like potential profile as shown in Fig. A.1 This enables us to reduce the problem of waves in a continuously varying potential to those within a constant potential. Together with appropriate boundary conditions, we link the solutions of neighboring step potentials, i.e., layers. Such waves are, of course, either sinusoidal or exponential.

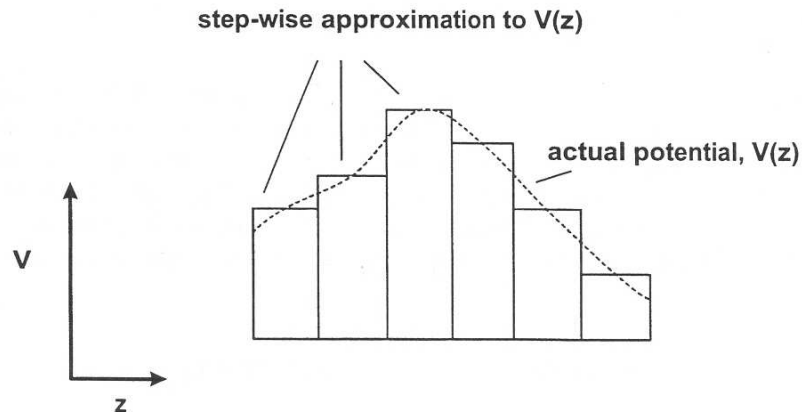


Figure A.1: Discretization of potential profiles in TMM.

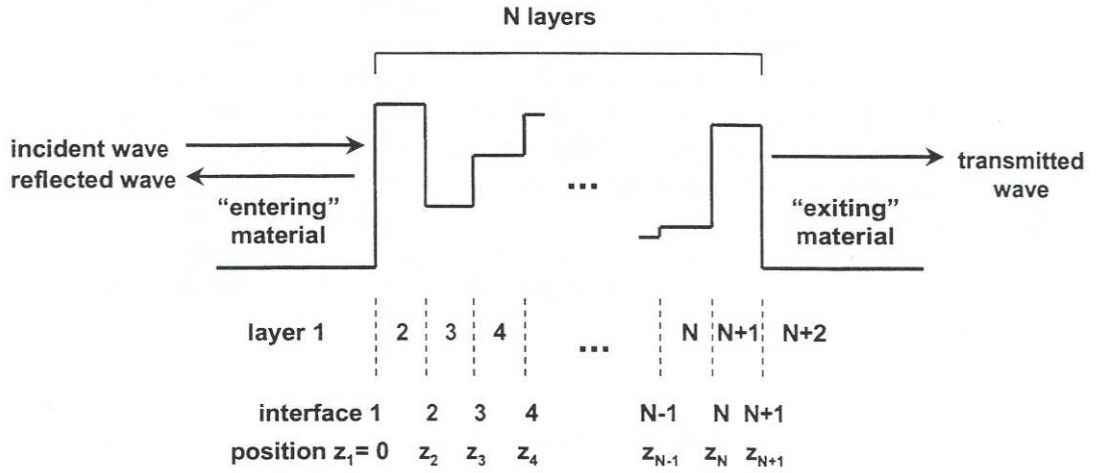


Figure A.2: Transfer matrix method nomenclature (After Ref. [14]).

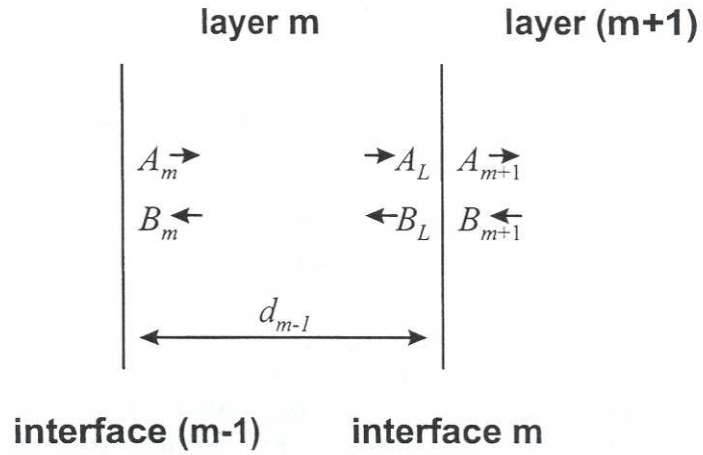


Figure A.3: Definition of waves for an arbitrary layer in TMM (After Ref. [14])

Assume that we have a potential structure modeled like the one in Fig. A.2. We can, as well, imagine that we have a *propagating* electron wave incident on the structure from one side, with a particular energy, E . In general, when a wave is incident on a structure, there will be some reflected wave and some transmitted wave.

To set up the formalism, we name each layer in the structure as given in Fig. A.2, and consider an arbitrary one as in Fig A.3. This approach will enable us to derive a matrix for every layer that relates the forward and backward amplitudes, A_m and B_m , just to the right of the $(m-1)$ th interface, to those of m th interface. By multiplying those matrices together, we will construct a “transfer matrix” for the whole structure, which will help us analyze the entire multilayer structure in a formal manner.

In our formalism, each layer m will have a constant potential energy V_m , a thickness d_m , and an effective mass m_{fm} . The position of the m th interface will be relative to the position of interface 1, which can be expressed as:

$$z_m = \sum_{q=2}^m d_{q-1} \quad (\text{A.1})$$

z_1 being 0.

For any given layer, m , if $E > V_m$, we will have a “forward” propagating wave of the form $A = A_0 e^{ik_m(z-z_m)}$, and a backward propagating wave of the form $B = B_0 e^{-ik_m(z-z_m)}$ (under the $e^{i\omega t}$ time evolution) where A and B are complex amplitude phasors representing the amplitude of the forward and backward waves, respectively. In this case k_m should be defined as:

$$k_m = \sqrt{\frac{2m_{fm}}{\hbar^2}(E - V_m)} \quad (\text{A.2})$$

under the effective mass approximation. Similarly for the case $V_m > E$, we will have a “forward” decaying wave of the form $A = A_0 e^{-\kappa_m(z-z_m)}$, and a “backward” decaying wave of the form $B = B_0 e^{\kappa_m(z-z_m)}$, where

$$\kappa_m = \sqrt{\frac{2m_{fm}}{\hbar^2}(V_m - E)} \quad (\text{A.3})$$

Now note that if we use only the form (A.2), we obtain an imaginary k ($\equiv i\kappa$) for the $V_m > E$. Mathematically, as long as we choose the positive square root (either real or imaginary) in both cases, we can only work with k ms. A forward propagating wave can then be fully and formally expressed as $e^{ik_m(z-z_m)} \equiv e^{-\kappa_m(z-z_m)}$. This will simplify our handling of mathematics of the problem. Now in any layer we have a wave that we can write as

$$\psi(z) = A_m e^{ik_m(z-z_m)} + B_m e^{-ik_m(z-z_m)} \quad (\text{A.4})$$

where k is given by Eq. (A.2).

Now we should set appropriate boundary conditions for adjacent layers. Using the notation of Fig. A.3, we have the continuity of the wavefunction, $\psi(z)$ and $d\psi/dz$ at the interface:

$$\psi = A_L + B_L = A_{m+1} + B_{m+1} \quad (\text{A.5})$$

$$\frac{d\psi}{dz} = ik(A - B) \quad (\text{A.6})$$

for the wave on either side of the boundary, so we have, for the right boundary in Fig. A.3,

$$A_L - B_L = \Delta_m(A_{m+1} - B_{m+1}) \quad (\text{A.7})$$

where

$$\Delta_m = \frac{k_{m+1}}{k_m} \quad (\text{A.8})$$

In a layered semiconductor structure under the effective mass approximation we can use the continuity of $(1/m_f)d\psi/dz$ for the second boundary condition, instead of Eq. (A.8) we obtain

$$\Delta_m = \frac{k_{m+1}}{k_m} \frac{m_{fm}}{m_{fm+1}}. \quad (\text{A.9})$$

We will use this Δ_m in Eq. (A.7) and all subsequent equations.

Using Eq. (A.5) and Eq. (A.7), we obtain the following for the amplitude at the exit of layer m

$$A_L = A_{m+1} \left(\frac{1 + \Delta_m}{2} \right) + B_{m+1} \left(\frac{1 - \Delta_m}{2} \right) \quad (\text{A.10})$$

and

$$B_L = A_{m+1} \left(\frac{1 - \Delta_m}{2} \right) + B_{m+1} \left(\frac{1 + \Delta_m}{2} \right) \quad (\text{A.11})$$

and this can be written in matrix form as

$$\begin{bmatrix} A_L \\ B_L \end{bmatrix} = \mathbf{D}_m \begin{bmatrix} A_{m+1} \\ B_{m+1} \end{bmatrix} \quad (\text{A.12})$$

where

$$\mathbf{D}_m = \begin{bmatrix} \frac{1 + \Delta_m}{2} & \frac{1 - \Delta_m}{2} \\ \frac{1 - \Delta_m}{2} & \frac{1 + \Delta_m}{2} \end{bmatrix} \quad (\text{A.13})$$

Having set the boundary conditions properly, we can now deal with the propagation that relates A_m and B_m to A_L and B_L . For the propagation in a given layer m , whose layer thickness is d_m , we have

$$A_m = A_L e^{-ik_m d_m} \quad (\text{A.14})$$

$$B_m = B_L e^{ik_m d_m} \quad (\text{A.15})$$

corresponding to matrix-vector equation

$$\begin{bmatrix} A_m \\ B_m \end{bmatrix} = \mathbf{P}_m \begin{bmatrix} A_L \\ B_L \end{bmatrix} \quad (\text{A.16})$$

with

$$\mathbf{P} = \begin{bmatrix} e^{-ik_m d_m} & 0 \\ 0 & e^{ik_m d_m} \end{bmatrix} \quad (\text{A.17})$$

Hence we can now write the full transfer matrix, \mathbf{T} , for the structure, which relates the forward and backward wave amplitudes at the “entrance” (i.e., just to the left of the first interface) to the forward and backward wave amplitudes at the exit (i.e., just to the right of the last interface),

$$\begin{bmatrix} A_1 \\ B_1 \end{bmatrix} = \mathbf{T} \begin{bmatrix} A_{N+2} \\ B_{N+2} \end{bmatrix} \quad (\text{A.18})$$

where

$$\mathbf{T} = \mathbf{D}_1 \mathbf{P}_2 \mathbf{D}_2 \mathbf{P}_3 \mathbf{D}_3 \cdots \mathbf{P}_{N+1} \mathbf{D}_{N+1} \quad (\text{A.19})$$

It is possible to use the transfer matrix itself to find eigenstates in the cases of truly bound states. For example, if the first (1) and last (N+2) layers are infinitely thick, their potentials are $V_1 > E$ and $V_{N+2} > E$ and for some m we have $V_m < V_1$ and $V_m < V_{N+2}$, there is at least one value of E for which there are bound eigenstates. Such states would only have exponentially decaying wavefunctions into the first and out of the last layer. Hence, $A_1=0$ and $B_{N+2}=0$. Therefore we must have

$$\begin{bmatrix} 0 \\ B_1 \end{bmatrix} = \mathbf{T} \begin{bmatrix} A_{N+2} \\ 0 \end{bmatrix} = \begin{bmatrix} T_{11} & T_{12} \\ T_{21} & T_{22} \end{bmatrix} \begin{bmatrix} A_{N+2} \\ 0 \end{bmatrix} \quad (\text{A.20})$$

which can only be the case if the element in the first row and first column of \mathbf{T} is zero, i.e.,

$$T_{11} = 0 \quad (\text{A.21})$$

and this can be used to search for eigenstates through varying E .

In the tunneling resonance method (TRM), we set up the *exit* vector so that there is no wave incident from the right. We then look for a transmission resonance from

left to right. Hence, we choose

$$\begin{bmatrix} A_{N+2} \\ B_{N+2} \end{bmatrix} = \begin{bmatrix} 1 \\ 0 \end{bmatrix} \quad (\text{A.22})$$

The choice for unit amplitude for A_{N+2} is arbitrary.

Now we can deduce what incident and reflected amplitudes must be

$$\begin{bmatrix} A_1 \\ B_1 \end{bmatrix} = \mathbf{T} \begin{bmatrix} 1 \\ 0 \end{bmatrix} \quad (\text{A.23})$$

So, the wave amplitude transmission of the structure ($1/T_{11}$) is then $1/A_1$. It is more convenient to look for a positive definite quantity when looking for a maxima, the most obvious one being intensity, $1/|A_1|^2$ ($1/|T_{11}|^2$).

If we search this maxima by changing E , using any search algorithm (e.g., bisection), we can get the energy eigenvalue(s). It is straightforward to find corresponding (resonant) eigenstate wavefunctions (and to normalize them) by using the matrices (\mathbf{D}_n and \mathbf{P}_n) defined throughout this formalism.

Bibliography

- [1] D. A. B. Miller and H. M. Ozaktas, “Limit to the Bit-Rate Capacity of Electrical Interconnects from the Aspect Ratio of the System Architecture”, *Special Issue on Parallel Computing with Optical Interconnects, J. Parallel and Distributed Computing*, vol. 41, p. 4252, 1997.
- [2] J. W. Goodman, F. I. Leonberger, S. Y. Kung, and R. A. Athale, “Optical Interconnections for VLSI Systems”, *Proceedings of IEEE* vol. 72, no. 7, p.p. 850–866, 1984.
- [3] G. A. Keeler, B. E. Nelson, D. Agarwal, and D. A. B. Miller, “Skew and jitter removal using short optical pulses for optical interconnection”, *IEEE Photonics Technology Letters*, vol. 12, pp. 714–716, 2000.
- [4] A. Bhatnagar, S. Latif, C. Debaes and D. A. B. Miller, “Pump-Probe Measurements of CMOS Detector Rise Time in the Blue”, *IEEE Journal of Lightwave Technology*, vol. 22, no. 9, pp. 2213–2217, 2004.
- [5] O. I. Dosunmu, D. D. Cannon, M. K. Emsley, B. Ghyselen, J. Liu, L. C. Kimerling, and M. S. Unlu, “Resonant Cavity Enhanced Ge Photodetectors for 1550nm Operation on Reflecting Si Substrates” *IEEE Journal of Selected Topics in Quantum Electronics*, vol. 10, no. 4, pp. 694–701, 2004.
- [6] S. L. Chuang, *Physics of Optoelectronic Devices*. Hoboken, NJ, USA: John Wiley and Sons Inc., 1995.
- [7] H. V. Demir, “Multifunctional Photonic Switches”, *Ph.D.Thesis* Department of Electrical Engineering, Stanford University, Stanford, USA, 2004.

- [8] N. C. Helman, “Optoelectronic Modulators for Optical Interconnects”, *Ph.D. Thesis* Department of Electrical Engineering, Stanford University, Stanford, USA, 2005.
- [9] Y. Dikme, “MOVPE and Characterization of GaN-based Structures on Alternative Substrates”, *Ph.D. Thesis* Faculty of Electrical Engineering and Information Technology, Aachen University, Aachen, Germany, 2006.
- [10] Z. Bougrioua, I. Moerman, L. Nistor, B. Van Daele, E. Monroy, T. Palacios, F. Calle, and M. Leroux, “Engineering of an insulating buffer and use of AlN interlayers: two optimisations for AlGaIn-GaN HEMT-like structures”, *Physica Status Solidi (a)*, vol. 195, no. 1, pp. 93–100, 2002.
- [11] V. Fiorentini, F. Bernardini, F. D. Sala, A. D. Carlo and P. Lugli, “Effects of macroscopic polarization in III-V nitride multiple quantum wells”, *Phys. Rev. B*, vol. 60, no. 12, pp. 8849–8858, 1999.
- [12] B. Monemar and G. Pozina, “Group III-nitride based hetero and quantum structures”, *Progress in Quantum Electronics*, vol. 24, pp. 230–290, 2000.
- [13] S. Nakamura, G. Fasol, and S. J. Pearton, *The Blue Laser Diode: The Complete Story*. Berlin, Germany: Springer-Verlag, 1997.
- [14] D. A. B. Miller, *Stanford University EE 343 Lecture Notes* Stanford, CA, USA: Stanford University, 1997.
- [15] B. E. A. Saleh, and M. C. Teich, *Fundamentals of Photonics*, Hoboken, NJ, USA: John Wiley and Sons Inc., 1991.
- [16] B. Butun, “Low Temperature Grown GaAs Based Resonant Cavity Enhanced Photodetectors”, *M.S. Thesis* Department of Electrical and Electronics Engineering, Bilkent University, Ankara, Turkey, 2004.
- [17] A. E. Oberhofer, “Gallium Nitride Ultraviolet Optical Modulators”, *Ph.D. Thesis* Department of Electrical and Computer Engineering, North Carolina State University, Raleigh, North Carolina, USA, 2004.
- [18] M. Honda, “Light Modulation Apparatus”, U.S. Patent Office, no. 3791717, 1974.

- [19] A. E. Oberhofer, J. F. Muth, M. A. L. Johnson, Z. Y. Chen, E. F. Fleet, and G. D. Cooper, “Planar gallium nitride ultraviolet optical modulator” *Applied Physics Letters*, vol. 83, no. 14, pp. 2748–2750, 2003.
- [20] D. A. B. Miller, D. S. Chemla, T. C. Damen, A. C. Gossard, W. Wiegmann, T. H. Wood and C. A. Burrus, “Electric Field Dependence of Optical Absorption near the Bandgap of Quantum Well Structures”, *Phys. Rev. B*, vol. 32, pp. 1043–1060, 1985.
- [21] H. V. Demir, V. A. Sabnis, O. Fidaner, J. S. Harris, Jr., D. A. B. Miller, and J.-F. Zheng, “Multifunctional integrated photonic switches”, *IEEE Journal of Selected Topics in Quantum Electronics*, vol. 11, no. 1, pp. 86–96, 2005.
- [22] I-H. Tan, G. L. Snider, L. D. Chang, and E. L. Hu, “A self-consistent solution of Schrodinger Poisson equations using a nonuniform mesh”, *Journal of Applied Physics*, vol. 68, no. 8, pp. 4071–4076, 1990.
- [23] K. Nakamura, A. Shimizu, M. Koshiha, and K. Hayata, “Finite-Element Analysis of Quantum Wells of Arbitrary Semiconductors with Arbitrary Potential Profiles” *IEEE Journal of Quantum Electronics*, vol. 25, no. 5, pp. 889–895, 1989.
- [24] H. Amano, N. Sawaki, I. Akasaki and Y. Toyoda, “Metalorganic vapor phase epitaxial growth of a high quality GaN film using an AlN buffer layer”, *Applied Physics Letters*, vol. 48, pp. 353-355, 1986.
- [25] O. Briot, S. Clur, and R. L. Aulombard, “Competitive adsorption effects in the metalorganic vapor phase epitaxy of GaN”, *Applied Physics Letters*, vol. 71, no. 14, pp. 1990–1992, 1997.
- [26] E. Sari, S. Nizamoglu, T. Ozel, and H. V. Demir, “Blue quantum electroabsorption modulators based on reversed quantum confined Stark effect with blueshift”, *Applied Physics Letters*, vol. 90, no. 1, pp. 011101-1–011101-3, 2007.
- [27] S. Nizamoglu, T. Ozel, E. Sari, and H. V. Demir, “White light generation using CdSe/ZnS core-shell nanocrystals hybridized with InGaN/GaN light emitting diodes” *Nanotechnology*, vol. 18, pp. 065709-1–065709-5, 2007.

- [28] I. Friel, C. Thomidis, and T. D. Moustakas, “Ultraviolet electroabsorption modulator based on AlGa_N/Ga_N multiple quantum wells”, *Journal of Applied Physics*, vol. 97, pp. 123515-1–123515-5, 2005.
- [29] M. Kneissl, T. L. Paoli, P. Kiesel, D. W. Treat, M. Teepe, N Miyashita, and N. M. Johnson, “Two-section InGa_N multiple-quantum-well laser diode with integrated electroabsorption modulator”, *Applied Physics Letters*, vol. 80, no. 18, pp. 3283–3285, 2002.
- [30] E. Sari, I. H. Lee, and H. V. Demir, *Manuscript in preperation*, 2007.